Marine and Petroleum Geology 148 (2023) 106069

Contents lists available at ScienceDirect

Marine and Petroleum Geology

journal homepage: www.elsevier.com/locate/marpetgeo

Effect of tectonic reworking on shale fracturing and gas preservation in the upper Yangtze block, south China

Qianqian Feng [a,b], Nansheng Qiu [a,b,*], Tenger Borjigin [c], Fei Li [d], Ruiyun Ji [a,b], Xin Liu [a,b], Yuanyuan Zhou [e], Aiqiang Cao [f], Gang Wang [g]

[a] State Key Laboratory of Petroleum Resources and Prospecting, China University of Petroleum, Beijing, 102249, China
[b] College of Geosciences, China University of Petroleum, Beijing 102249, China
[c] Oil and Gas Survey Center of China Geological Survey, Beijing 100083, China
[d] Sinopec Exploration Company, Chengdu 610041, China
[e] Wuxi Research Institute of Petroleum Geology, Sinopec Petroleum Exploration and Production Research Institute, Wuxi, 214126, China
[f] PetroChina No.2 Gas Production Plant, Changqing Oilfield Company, Yulin 719000, China
[g] PetroChina Qinghai Oilfield Company Petroleum Exploration and Development Institute, Dunhuang 736200, China

ARTICLE INFO

Keywords:
Tectono-thermal evolution
Low-temperature thermochronology
Pressure evolution
Shale gas preservation
Upper yangtze block

ABSTRACT

Lower Silurian shale, with a variable gas enrichment, in the Upper Yangtze Block is used to evaluate the response of shale fracturing and gas loss to differential tectonic reworking. The Meso-Cenozoic uplift process was reconstructed by apatite fission track, zircon fission track, apatite (U–Th)/He and zircon (U–Th)/He dating. During the Mesozoic, due to Pacific-Eurasian convergence the Upper Yangtze Block underwent northwestward progressive deformation, with a periodic uplift process characterized by rapid uplift during the Early-Late Cretaceous, followed by subsequent slow uplift. The Cenozoic uplift process was characterized by rapid uplift in the Sichuan Basin as a result of Indian-Asian collision and inherited slow uplift in the Hubei–Hunan–Guizhou fold belt in response to Pacific-Eurasia convergence. The pressure evolution of the Lower Silurian shale was reconstructed using fluid inclusions and variation in shale gas content was quantified. By comparing the differences in pressure reduction, fracturing, and shale gas loss we explore the effect of tectonic reworking on shale fracturing and gas preservation in relation to deformation, uplift and the maximum burial depth. Deformation increases fracture development and reduces the sealing capacity of the shale. Uplift amplitude is a major controlling factor. Large amounts of uplift resulted in clear fracturing and massive gas loss. Triaxial fracture tests show that the maximum burial depth is associated with shear fractures in the shale and thereby affects shale gas preservation during uplift. The differences of slip deformation, tectonic uplift amplitude and the maximum burial depth of shale resulted in the differential enrichment of the Lower Silurian shale gas.

1. Introduction

As an unconventional natural gas stored in shale, shale gas has recently become a key exploration target in many countries, including the United States, Canada, and China. It occupies a key position in the world energy industry (Assad et al., 2018; Yang et al., 2021). With the development of shale gas exploration and development, shale fracturing and gas preservation conditions have become the core issues of increasing concern. Shale reservoirs are complicated dual-porosity media systems composed of abundant pores and microfractures, which act as the storage spaces and main transport pathways of the shale gas. The degree of shale fracturing is a controlling factor of gas producibility, and tectonic events are one of the main mechanisms causing fracture growth and play an important role in shale gas preservation (Slatt and O'Brien, 2011; Zeng et al., 2013; Ougier-Simonin et al., 2016). Triaxial fracturing tests have revealed that uplift changes shale from plastic to brittle, resulting in shear fracturing (Nygård et al., 2006; Chen et al., 2016; Ju et al., 2018; Tan et al., 2020). The regional fractures in the Upper Triassic shale in central China, the Lower Silurian shale in southern China, as well as the Antrim Shale, Albany Shale, and Lewis

Abbreviations: UYB, Upper Yangtze Block; R_o, vitrinite reflectance; R_{equ}, equivalent vitrinite reflectance; TOC, total organic carbon; AFT, apatite fission track; ZFT, zircon fission track; AHe, apatite (U-Th)/He; ZHe, zircon (U-Th)/He.

* Corresponding author. State Key Laboratory of Petroleum Resources and Prospecting, China University of Petroleum, Beijing, 102249, China.
E-mail address: qiunsh@cup.edu.cn (N. Qiu).

https://doi.org/10.1016/j.marpetgeo.2022.106069
Received 23 November 2021; Received in revised form 16 October 2022; Accepted 8 December 2022
Available online 10 December 2022

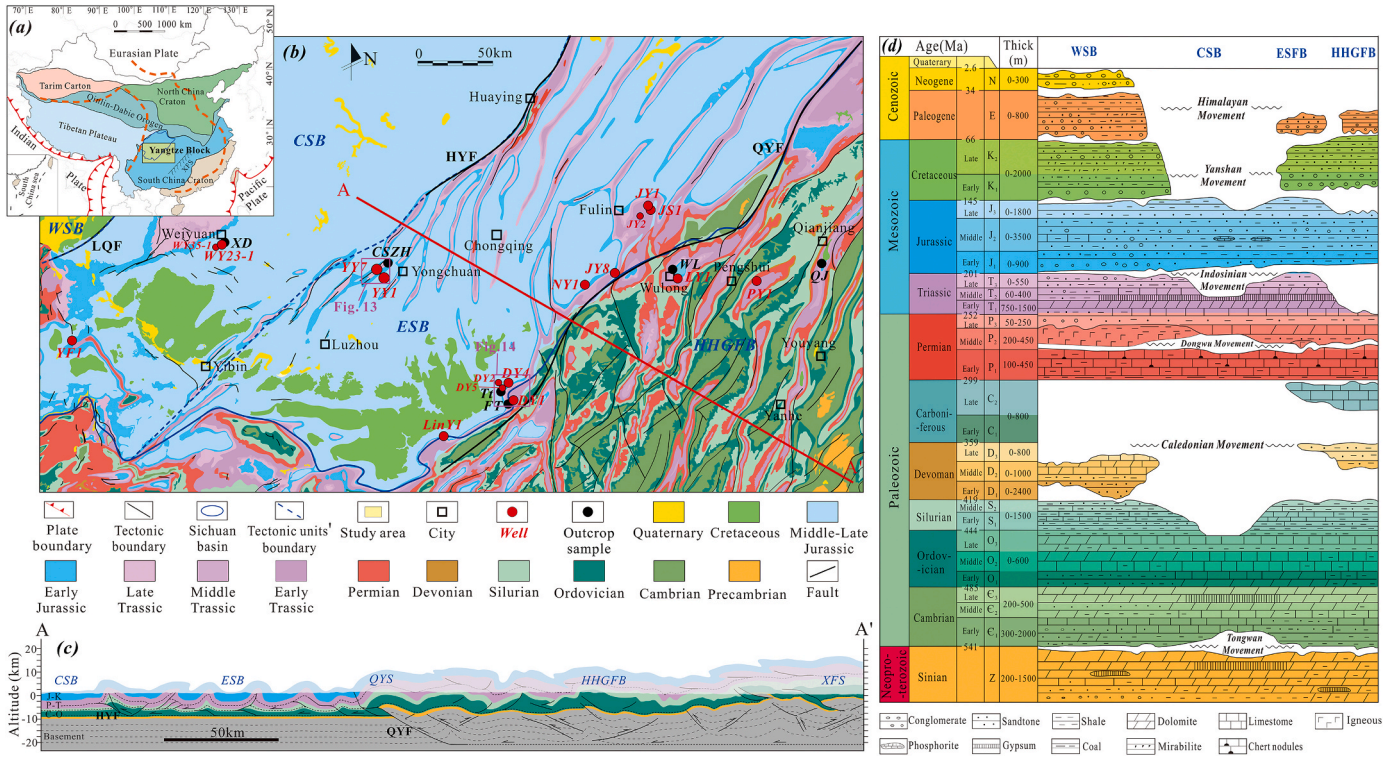

Fig. 1. (a) The tectonic location of the Upper Yangtze Block (modified after Jiang et al. (2019)), XFS–Xuefengshan; (b) geologic map of the Upper Yangtze Block. HYF–Huayingshan Fault, QYF–Qiyueshan Fault, LQF–Longquanshan Fault, QYF–Qiyueshan, HHGFB–Hubei-Hunan-Guizhou Fold Belt, ESB–eastern Sichuan Basin, CSB–central Sichuan Basin, WSB–western Sichuan Basin. (c) Structural section of cross-section A-A', the plane location is shown in (b); (d) stratigraphic column and tectonic movements in the Upper Yangtze Block (modified after Liu et al. (2016); Wang et al. (2021)).

Shale in North America are all considered to be related to uplift (Curtis, 2002; Julia et al., 2014; Ding et al., 2016; Li et al., 2020; Ge et al., 2021). With proven gas reserves of more than 1 trillion m^3, the Upper Yangtze Block (UYB) is the primary shale gas-producing region in China. As of December of 2021, the total production exceeded 500 × 10^8 m^3 (20 °C, 101 KPa) (He et al., 2020; Ma et al., 2021). Exploration practices have revealed that there are significant variations in the gas content of the Lower Silurian shale in the UYB and the gas preservation conditions are the key factor controlling the differential enrichment of shale gas (Guo and Zeng, 2015; Guo et al., 2017; Ma et al., 2018; Li et al., 2020; Shu et al., 2020). Moreover, the UYB experienced multiple stages of tectonic movement, resulting in significant differential uplift of the Lower Silurian shale (Yan et al., 2003; Richardson et al., 2008; Shen et al., 2009; Deng et al., 2013; Wu et al., 2020; Liu et al., 2021a). It is generally believed that the strength and duration of tectonic reworking is the major factor controlling shale gas preservation conditions and determines the gas contents of shale reservoirs (Hu et al., 2014; Guo et al., 2017; He et al., 2020; Li et al., 2020). In addition, the shale gas loss due to the uplift during the Variscan Orogeny possesses a major geological challenge in the exploration and development of the Mississippi Alum shale occurs in northern Europe (Assad et al., 2018). The folded and faulted, with gentle to steep layer dips and structural complexity, constrain U.S. shale gas production, including the Miocene Monterey, Middle Devonian Marcellus, and the Eagle Ford shales (Evans et al., 2014; Ferrill et al., 2014; Wilkins et al., 2014). Therefore, the effect of tectonic reworking on shale fracturing and gas preservation is a core scientific issue in the shale gas industry.

Previous studies have intensively analyzed the effect of tectonic reworking on shale fracturing and gas preservation from the perspectives of the faulting intensity, structural style, fracture growth, and intensity and duration of the late tectonic uplift (Zeng et al., 2013; Evans et al., 2014; Ferrill et al., 2014; Guo et al., 2017; Wei et al., 2017; He et al., 2019, 2020). A broad and gentle structure with a continuous seal, moderate fracture growth, appropriate distance to the fault zone, and late uplift is conducive to shale gas preservation and exploitation (Smart et al., 2014; Guo et al., 2017; Ma et al., 2018; He et al., 2019). However, these studies were mostly based on qualitative analysis of static parameters, such as faulting intensity, structural style, intensity and duration of the late tectonic uplift, etc. The response of shale fracturing and gas loss to different tectonic reworking events is still not clear. Shale gas loss during uplift lacks quantitative characterization. It is necessary to further study the dynamic loss of shale gas during tectonic evolution. By studying the tectono-thermal evolution, the uplift processes can be reconstructed. The burial history, hydrocarbon generation history, and temperature and pressure evolution of the shale can be further reconstructed, providing a framework for the dynamic evaluation of shale gas preservation.

In this study, the effect of tectonic reworking on shale fracturing and gas preservation was investigated through a case study of the Lower Silurian shale with variable gas enrichment in the UYB, southwestern China. First, the Meso-Cenozoic uplift process was reconstructed based on vitrinite reflectance (R_o) and low-temperature thermochronology data, including apatite fission track (AFT), zircon fission track (ZFT), apatite (U–Th)/He (AHe), and zircon (U–Th)/He (ZHe) data. Then, we estimated the pressure evolution of the Lower Silurian shale through fluid inclusion analysis and basin modeling. Based on the temperature and pressure evolution, the variation in the shale gas content was quantitatively characterized. Finally, combined with the results of triaxial fracturing tests conducted on the Lower Silurian shale and the differences in pressure decrease process, the fracturing, shale gas lose, and the effect of the tectonic reworking on shale gas preservation were investigated from the perspectives of slip deformation, uplift, and maximum burial depth. In addition to quantitatively assessing the effects of the tectonic reworking on the shale fracturing and gas preservation, this study provides a scientific basis for analyzing the differential enrichment mechanism of shale gas. The results of this study also have

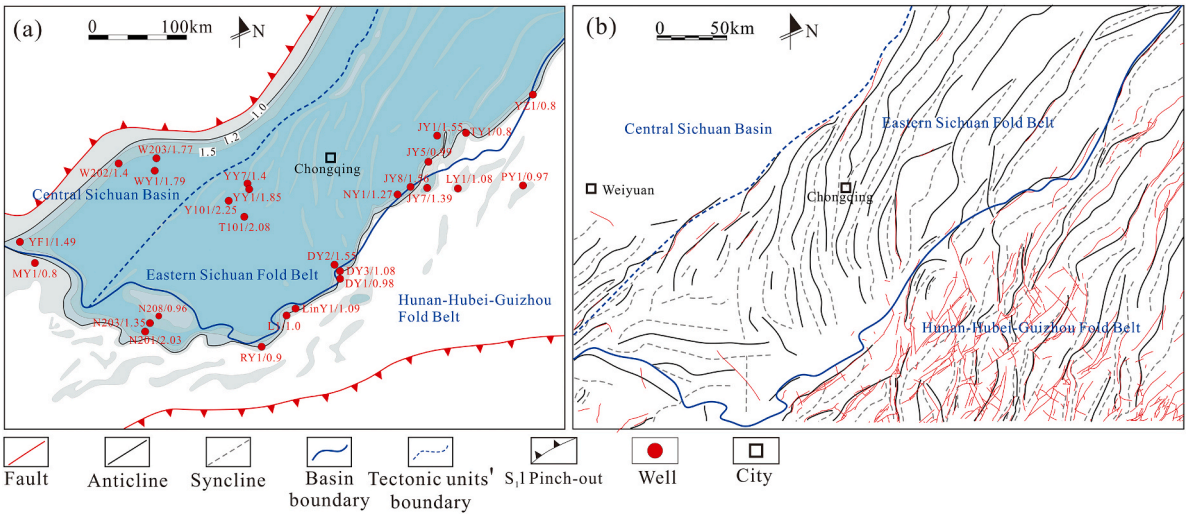

Fig. 2. (a) Pressure distribution characteristics of the Lower Silurian strata in the Upper Yangtze Block; DY2/1.55: the pressure coefficient of the Lower Silurian strata in Well DY2 is 1.55. (b) The fold and fault distribution characteristics of the Lower Silurian strata in the Upper Yangtze Block.

important implications for shale gas exploration and development around the world.

2. Geological setting

The UYB is located in the western part of the South China Block and comprised the Sichuan Basin and the Hubei–Hunan–Guizhou fold belt. Tectonically, it is bounded by the Qinling Orogen to the north, the Tibetan Plateau to the west, and the Xuefengshan thrust belt to the east (Fig. 1a). Within the UYB, a large-scale intracontinental thrust system is separated from the central Sichuan Basin by the Huayingshan Fault (Fig. 1b). The fold-and-thrust belt with multiple detachments is well developed and exhibits different structural styles. Separated by the Qiyueshan Fault, it varies from the eastern Sichuan Basin, which is represented by subparallel chevron anticlines, in the west to the Hubei–Hunan–Guizhou fold belt, which is dominated by chevron synclines, in the east (Fig. 1c). There is a thrust nappe structure in the Qiyueshan area near the eastern boundary of the Sichuan Basin (Fig. 1b and c). Owing to their abundant gas reserves, the western slope of the central Sichuan Basin, the eastern Sichuan Basin, and the synclines in the Hubei–Hunan–Guizhou fold belt are the key areas of shale gas exploration in China. Significant gas fields have been discovered in the Lower Silurian shale including the Fuling, Weiyuan, Dingshan, Yongchuan, and Chingning shale gas fields.

The Paleozoic to Cenozoic stratigraphic succession can be divided into two main depositional intervals: the marine sequence from the Paleozoic to the Middle Triassic and the terrestrial sequence from the Late Triassic to the Eocene (Fig. 1d). The sedimentary cover has a total thickness of 5–10 km (Ma, 2007; Liu et al., 2021a). As the main shale gas rich reservoir, the Lower Silurian is mainly composed of black organic-rich shale containing abundant graptolites with a thickness of 30–120 m. The overlying caprock composed of the Middle Silurian green silty mudstone and the underlying floor of the Middle Ordovician dark gray limestone have good sealing abilities. With a distribution area of $>10 \times 10^4$ m^3, the shale has burial depths of 1300–4500 m (Zou et al., 2015). The total organic carbon (TOC) content ranges from 0.4% to 18.4%, with an average of 2.5%; and the high TOC sections (TOC >2%) are mainly developed in the lower part of the Lower Silurian. The shale is highly mature, with R_o values ranging from 2.4% to 3.63% (Wang et al., 2019). The pressure coefficient of the Lower Silurian ranges from 1.0 to 2.5. The pressure coefficient in the Hubei–Hunan–Guizhou fold belt is generally less than 1.0, while the Lower Silurian in the Sichuan Basin is characterized by overpressure (Fig. 2a). Exploration has shown

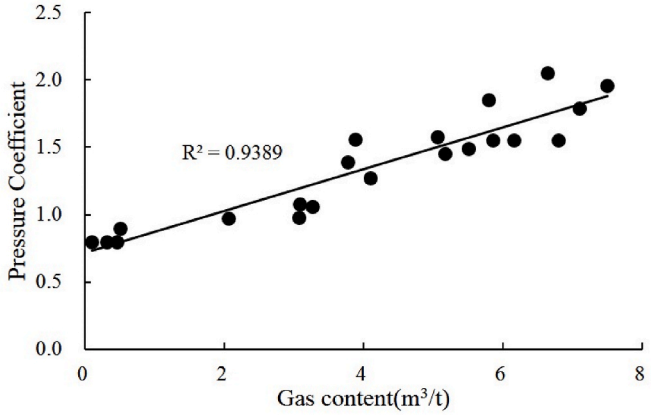

Fig. 3. Correlation between the gas content and the pressure coefficient for the Lower Silurian strata in typical wells.

that the pressure is a comprehensive indicator of the preservation conditions and has an obvious positive correlation with the shale gas content (Fig. 3). Therefore, the increase in the pressure coefficient from the Hubei–Hunan–Guizhou fold belt to the Sichuan Basin suggests that the UYB is characterized by differential shale gas enrichment.

Located in the transition zone between the Tethys-Himalayan tectonic domain and the Circum-Pacific tectonic domain, the UYB experienced multiple tectonic stages from the Paleozoic to the Cenozoic, including the Caledonian, Hercynian, Indosinian, Yanshanian, and Himalayan movements. These tectonic movements resulted in a complex fault and fold system (Fig. 2b), the absence of most of the upper Silurian, Devonian, and Carboniferous strata across the South China Craton; the E-W-trending Leshan-Longnvshi paleo-uplift in the central Sichuan Basin, and several regional unconformities (Fig. 1d). The fold and fault distribution characteristics indicate that the structural form of the UYB was mainly controlled by SE-NW compression during the Yanshanian movement (Early Cretaceous-Eocene) and the approximately E-W compression during the Himalayan movement (Eocene-present time) (Deng et al., 2013; Wang et al., 2014; Yong et al., 2018; Liu et al., 2021a). The Jurassic and Triassic strata are mainly exposed in the Sichuan Basin, while the strata exposed in the Hubei–Hunan–Guizhou fold belt are mainly Cambrian to Ordovician in the anticlines and Silurian to Permian in the synclines. Thermochronology and laboratory simulation experiments have shown that the UYB experienced

Table 1
Details of the thermochronology samples and the measured ZFT and AFT ages.

Fission-track	Sample	Stratigraphic	Lithology	Elevation /Depth(m)	Grains	P (χ2)	Central Age (Ma) (±1σ)	MTL ± SD (μm) (N)	Dpar (μm)
AFT	XD	J_2 (174–163 Ma)	Sandstone outcrop	389	40	0.57	52.6 ± 11.5	12.12 ± 2.62 (66)	1.68
	YY1	J_2 (174–163 Ma)	Sandstone cuttings	−316	38	0.82	56.0 ± 12.5	11.14 ± 2.19 (33)	1.63
	CSZH1	T_3 (235–201 Ma)	Sandstone outcrop	374	12	0.17	48.6 ± 14.7	11.25 ± 2.45 (14)	1.51
	JY8	S_1 (438–433 Ma)	Sandstone cuttings	−2254	26	1.00	18.7 ± 5.3	12.20 ± 2.14 (26)	1.63
	WL	J_2 (174–163 Ma)	Sandstone outcrop	678	34	0.63	90.9 ± 11.7	12.54 ± 1.71 (52)	1.9
	QJ	J_2 (174–163 Ma)	Sandstone outcrop	490	27	0.43	98.0 ± 12.7	13.12 ± 2.02 (77)	1.78
	LingY1	T_3 (235–201 Ma)	Sandstone cuttings	−318	15	0.68	62.4 ± 13.5	12.55 ± 1.79 (9)	1.85
	Tt	J_2 (174–163 Ma)	Sandstone outcrop	1077	27	0.45	66.6 ± 4.7	12.0 ± 2.02 (41)	2.12
	FT	J_2 (174–163 Ma)	Sandstone outcrop	835	24	0.93	69.3 ± 5.2	12.0 ± 1.71 (41)	2.04
	YF1-2	T_3 (235–201 Ma)	Sandstone cuttings	−436	40	0.82	48.2 ± 3.4	12.08 ± 1.79 (21)	1.63
ZFT	JS1	ϵ_1 (514–509 Ma)	Sandstone cuttings	−3925	35	0	242.2 ± 10.8		
	YF1	ϵ_1 (514–509 Ma)	Sandstone cuttings	−4413	34	0	205.3 ± 8.8		

P(χ2) is chi-square probability (Galbraith, 1981). MTL is Mean track length. SD is the standard deviation of measured confined track lengths. N is the number of track lengths. Dpar is long axis of track etch pit, which is usually used as a proxy for the influence of chemical composition on track annealing (Donelick et al., 2005). ZFT data are obtained from Feng et al. (2021).

progressive northwestward tectonic deformation from the Hubei–Hunan–Guizhou fold belt to the Sichuan Basin from ~170 Ma to ~90 Ma (Richardson et al., 2008; Shen et al., 2009; Shi et al., 2016; Liu et al., 2018; Wu et al., 2020). The uplift of the Qiyueshan area occurred at ~120 Ma, while the central uplift occurred at about 90–100 Ma. The thermal histories reconstructed using low-temperature thermochronology data demonstrate that the UYB experienced periodic uplift characterized by rapid uplift from the Late Jurassic/Early Cretaceous to the Late Cretaceous, slow uplift during the Late Cretaceous-Oligocene, and rapid uplift since the Oligocene. The fold and fault distribution and stratigraphic exposure characteristics indicate that obvious differential tectonic reworking and denudation have occurred in the UYB since the Mesozoic. The UYB is an excellent area for analyzing the effects of tectonic reworking on shale gas preservation due to the coupling of the differential tectonic reworking and the differential enrichment of shale gas. Twelve wells with different gas contents in the Lower Silurian shale were selected for the analysis, including wells WY23-1 and YF1 in the central Sichuan Basin; wells JY1, JY8, NY1, YY1, YY7, LingY1, DY4, and DY1 in the eastern Sichuan Basin; and wells LY1 and PY1 in the Hubei–Hunan–Guizhou fold belt (Fig. 1b).

3. Samples, methods and results

3.1. Low-temperature thermochronology

In this study, cutting and core samples from 12 shale gas wells were selected for AFT, ZFT, AHe, and ZHe analyses to reconstruct the Meso-Cenozoic uplift process. The detailed sample locations and lithology data are presented in Table 1 and Fig. 1b. Fission track thermochronology is based on the retention of radiation damage due to the spontaneous fission of ^{238}U in uranium-bearing minerals (commonly apatite or zircon) (Donelick et al., 2005). ZFT can be used to reconstruct the thermal history of a rock sample through the partial annealing zone of ~170–350 °C (Bernet, 2009), while AFT is characterized by a partial annealing zone in the range of ~60–125 °C (Gleadow et al., 1986; Green et al., 1986; Ketcham et al., 2007; Fitzgerald and Malusà, 2018). (U–Th)/He thermochronology is a method based on the He produced from the nuclear decay of the U and Th in accessory minerals. Systematic diffusion studies have shown that the ZHe partial annealing zone is ~140–200 °C (Reiners, 2005) and the AHe partial annealing zone is ~40–75 °C (Wolf, 1998). Based on the different thermochronology data, the thermal history of the samples from different regions and layers was determined.

The fission-track thermochronology analyses were conducted at the Thermochronology Laboratory of the China University of Petroleum, Beijing. AFT analysis was conducted on samples XD, YYI, CSZH, JY8, WL, QJ, LingY1, Tt, FT, and YF1-1, and we determined the ZFT ages of samples YF1-2 and JS1. The AFT ages of samples Tt and FT were determined using the external detector method and ζ(zeta) calibration (Hurford and Green, 1983). The Trackkey software (Dunkl, 2002) was used to calculate the fission track ages based on a zeta-value of 268.6 ± 13.4 a/cm^2. The testing procedure was the same as that described by Chang et al. (2019b). The AFT ages of the other eight samples were obtained using laser ablation inductively coupled plasma mass spectrometry (LA-ICP-MS) by technique described by Cogné et al. (2020). The fission tracks were counted using a Zeiss Axio-Imager M2m microscope and the TrackWorks software (Dunkl, 2002). For each sample, the grains with polished surfaces parallel to the c-crystallographic axis were selected for analysis. The horizontal confined track lengths and three Dpar were measured for each counted grain as a proxy for the compositional influence on the annealing of each counted grain. The uranium content of each analyzed grain was also measured following the procedure described by Cogné et al. (2020). Additional compositional data for a subset of elements (e.g., ^{43}Ca, ^{238}U, ^{232}Th, ^{35}Cl, ^{37}Cl, ^{204}Pb, and ^{207}Pb) were also obtained. The ^{43}Ca content was used as the internal standard element, and the AFT age was calculated based on the Durango apatite age standard. The detailed information of the ZFT analysis is described in our previous study (Feng et al., 2021). The RadialPlotter and DensityPlotter programs (Vermeesch, 2009, 2012) were used to create the probability density plot and the kernel density estimators. The RadialPlotter software identifies and extracts the component ages from mixed age populations. For each sample, the grain age distributions were decomposed into discrete main age components using a mixture modeling algorithm and were manually selected after the fission track data were log transformed following the method of Galibraith and Green (1990).

The AHe age analysis was performed on the Mesozoic samples (XD, YY1, CSZH1, JY8, WL, QJ, LingY1, Tt, FT and YF1-2) at the University of Florida following the procedures described by Chang et al. (2019a). The ZHe analysis of the zircon grains from samples YF1, JS1, FT, WL, and QJ was conducted at the School of Earth Science, University of Melbourne, following the procedures described by Gleadow et al. (2015). For each sample, five apatite and zircon grains were analyzed.

3.2. Vitrinite reflectance data

The maturity of the organic matter is controlled by the maximum paleotemperature, and the vitrinite reflectance (R_o) is the most commonly used indicator (Taylor et al., 1998; Suárez-Ruiz et al., 2012; Hackley and Cardott, 2016). Because vitrinite is absent in the Lower Paleozoic stratum, the equivalent R_o (R_{equ}) data have been used based on the vitrinite-like maceral reflectance (R_v), graphite reflectance (R_g), or bitumen reflectance (R_b). Here, the formulas calculating R_{equ} are obtained from R_b (Feng and Chen, 1988; Wei et al., 2016; Schmidt et al.,

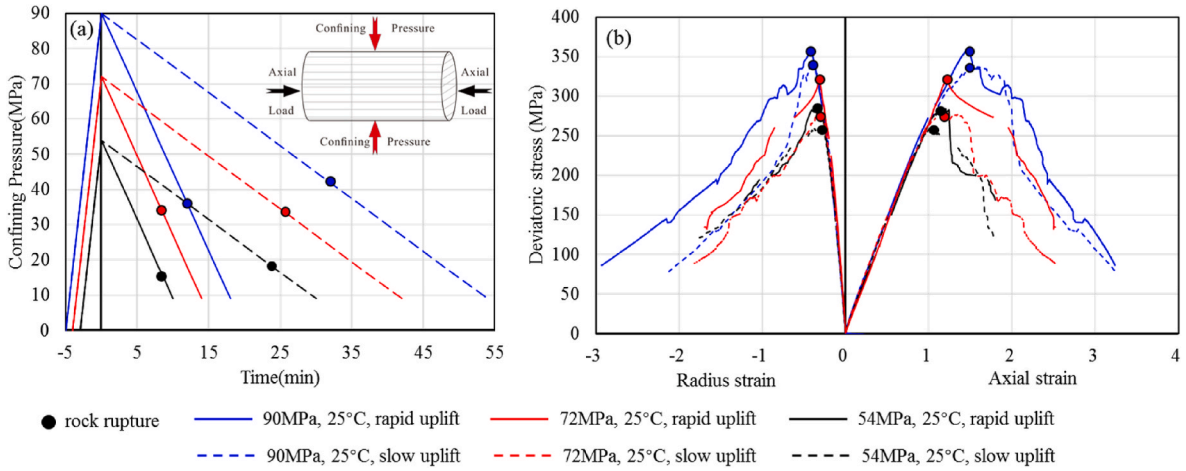

Fig. 4. (a) The loading and unloading of the confining pressure; (b) stress–strain curves of the shale samples during the unloading process. The points represent the rock rupture points.

2019) and R_g (Petersen et al., 2013; Wang et al., 2019; Luo et al., 2020). The R_{equ} data for the dark shale cuttings from 9 wells (YY1, YY7, LingY1, PY1, LY1, NY1, JY8, JY1, and WY23-1) were measured at the Wuxi Research Institute of Petroleum Geology following the method described by Littke et al. (2012). The R_{equ} data for six wells (DS1, DY2, DY5, JS1, WY35-1, and YF1) were compiled from Feng et al. (2021), Qiu et al. (2021) and Wang et al. (2021).

3.3. In-situ Raman shifts of inclusions

The pressure evolution of the Lower Silurian strata is constrained by the capture pressure of the fluid inclusions obtained from their in-situ Raman shifts. The Raman shifts of certain substances have a good relationship with temperature and pressure, and thus, the function of the correlation between the Raman shifts and temperature–pressure can be established by measuring the difference in the Raman shifts at different temperatures in a closed system (Thomas et al., 1990; Lu et al., 2007; Wang et al., 2011). In this study, the inclusion data for wells YY1, YY7, PY1, NY1, JY1, and DY4 were obtained from the Wuxi Research Institute of Petroleum Geology, Sinopec Petroleum Exploration & Production Research Institute. Fractures are filled with blocky calcite and/or blocky quartz in the Lower Silurian stratigraphic intervals. Quartz cement were observed either as the only cement present, or as a cement phase post-dating earlier calcite cement (Fig. 1 in the Supplemental Material S1). Single-phase methane inclusions were observed in all the samples, whereas aqueous two-phase inclusions were consistently observed alongside methane inclusions in several crystals of each sample. The inclusion photographs and Raman spectroscopy are shown in the Supplemental Material S1. The internal pressure and density at 20 °C were calculated based on the corrected Raman shifts of the CH_4 inclusions in the quartz and calcite veins in the Lower Silurian shale. The coexistence of the methane and aqueous inclusions within the same fluid inclusion assemblage indicates that fluid inclusions were trapped in the two-phase immiscible field. The minimum value of homogenization temperature of coexisting gas-liquid inclusion represents the trapping temperature of the methane inclusion. We followed the technique of Lu et al. (2007) to determine the density within individual methane inclusion using Raman spectroscopic analyses. The trapping pressure was calculated on the basis of the density of methane inclusions, trapping temperature, and the equation of state for supercritical methane by Duan et al. (1992). Furthermore, the burial depth and trapping time were obtained from the burial history of the Lower Silurian shale using the trapping temperatures.

3.4. Triaxial fracturing test

Triaxial fracturing tests were used to identify the strain characteristics of the Lower Silurian shale at different maximum burial depths (3000 m, 4000 m, and 5000 m) during the unloading process. In this study, different confining pressures were set to simulate the maximum burial depths and different unloading rates were set to simulate the uplift durations. As the effective overlying formation pressure, the confining pressure (P_c, MPa) was calculated using the following equation:

$$P_c = D_{max} \times (\rho_f - \rho_w), \quad (1)$$

where D_{max} is the maximum burial depth (m); ρ_f is the skeleton density of the overlying strata (2.8×10^3 kg/m^3); and ρ_w is the density of the formation water (1×10^3 kg/m^3). The confining pressures for maximum burial depths of 3000 m, 4000 m, and 5000 m were 54 MPa, 72 MPa, and 90 MPa, respectively. The samples were obtained from a large irregular shale outcrop in the eastern Sichuan Basin (106°55′57.74″ E, 28°53′08.83″ N), thereby guaranteeing that all of the samples had the similar mechanical properties. The experiments were conducted in the Institute of Acoustics, Chinese Academy of Sciences. The weathered surfaces of the outcrop were removed, and each final testing block was a 50 mm high cylinder with a diameter of 25 mm. In all of the experiments, the axial loading rate was 0.18%/min, while the confining pressures were initially loaded at a rate of 18 MPa/min and then were unloaded at the rate of 4.5 MPa/min and 1.5 MPa/min (Fig. 4a).

4. Results

4.1. Tectono-thermal evolution

4.1.1. Thermochronological ages

The fission-track data are presented in Table 1 and the detrital apatite and zircon fission track results are shown in Fig. 5. The AFT central ages of the samples, ranging from 21.0 ± 3.1 Ma to 100.4 ± 7.2 Ma, are significantly younger than their stratigraphic ages, which indicates that these samples likely remained in the AFT partial annealing zone during the Meso-Cenozoic. The P (χ2) values are all greater than 5% and the percentage dispersion is small, with a value of 0–25%, indicating the provenance of the similar grains. The distributions of the fission track grain ages were all decomposed into one age peak. Therefore, by determining the confined track length distribution of the sample, we can define whether the sample is composed of grains that have all rapidly cooled and thus whether the age peak represents a simple

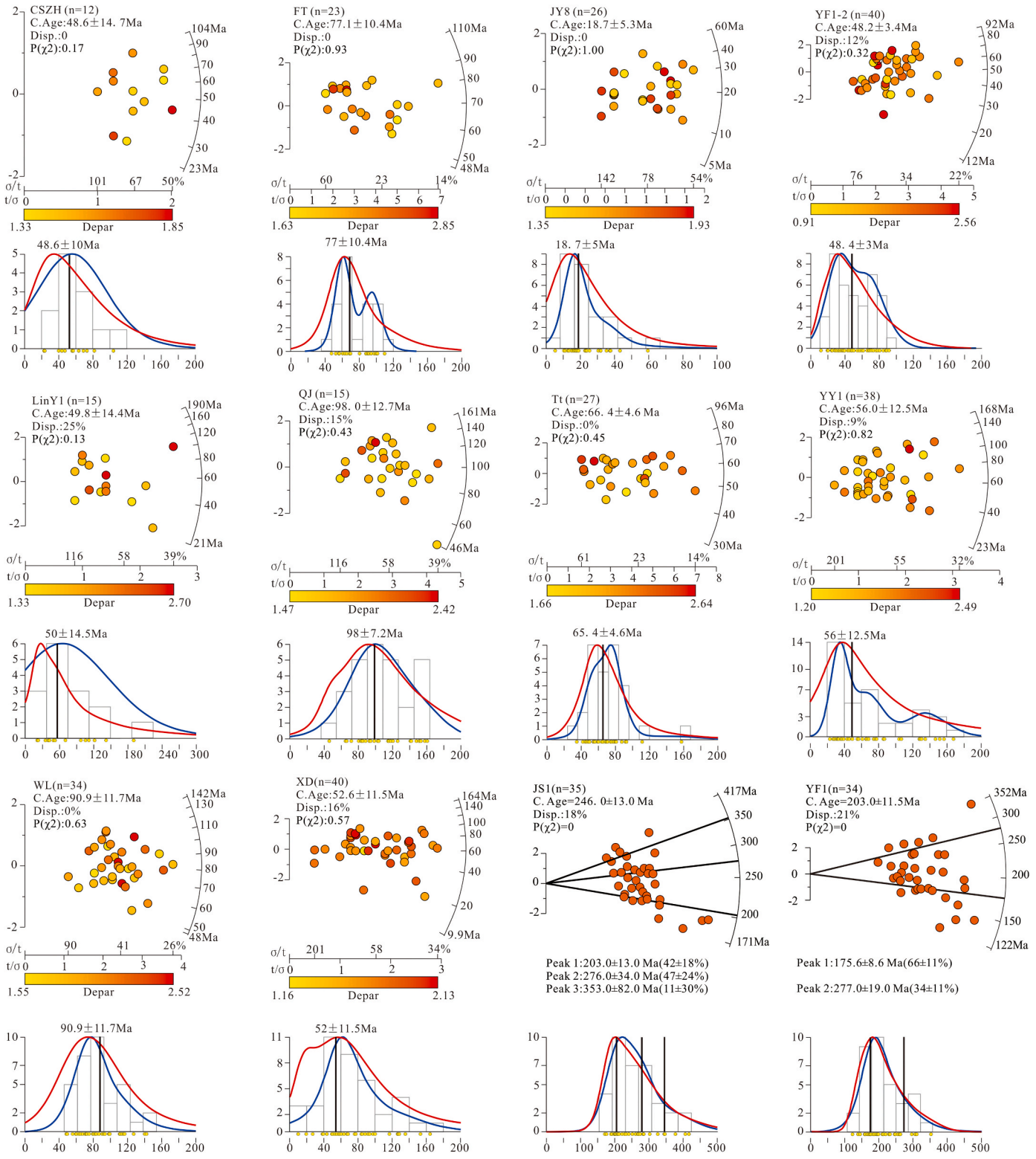

Fig. 5. Detrital apatite and zircon fission track results. Radial plots of the single grain age data, probability density plots (PDPs) (red line), and kernel density estimate (KDE) (blue line) of the fission track grain age distributions using the Radial Plotter and Density Plotter programs (Vermeesch, 2009, 2012). C. Age–Central age; Disp.–Dispersion. (For interpretation of the references to colour in this figure legend, the reader is referred to the Web version of this article.)

rapid cooling/exhumation event. The mean track lengths of the samples range from 11.14 ± 2.19 μm to 13.12 ± 2.02 μm, and the Depar ranges from 1.51 to 2.12 μm, indicating slow cooling through the AFT partial annealing zone. The single-grain ages and Dpar values do not exhibit a positive correlation, which indicates that the ages do not reflect kinetic variations. The age variation more likely represents the distribution of the bedrock AFT ages within the catchments. Therefore, we conclude that the AFT central ages reflect a rapid cooling event in the UYB. The thermal information for the ZFT ages of samples YF1-2 and JS1 was described in our previous study (Feng et al., 2021).

Table 2
The measured AHe ages.

Sample	Radius (μm)	^{4}He (nmol■g^{-1})	Mass (μg)	FT	U (ppm)	Th (ppm)	eU (ppm)	Corrected age (±1σ) (Ma)
XD-1	34.9	4.2	1.1	0.6	29.6	48.2	41.0	32.1 ± 1.8
XD-2	32.1	5.0	0.9	0.6	36.3	34.9	44.5	36.6 ± 2.0
XD-3	37.7	10.3	1.3	0.6	38.1	5.3	39.4	76.5 ± 4.3
XD-4	39.2	1.9	1.1	0.6	8.4	9.9	10.7	32.7 ± 2.0
XD-5	36.6	3.2	0.9	0.6	25.5	25.3	31.4	18.8 ± 1.1
XD-6	44.3	0.5	1.4	0.7	5.2	1.9	5.7	16.0 ± 1.3
YY1-1	33.9	2.5	0.8	0.6	23.2	5.0	24.4	18.5 ± 1.0
YY1-2	35.6	2.0	1.0	0.6	17.3	30.0	24.3	15.1 ± 0.9
YY1-3	44.0	0.8	1.6	0.7	4.4	29.2	11.3	13.2 ± 0.7
YY1-4	37.8	6.9	1.1	0.6	58.8	50.1	70.6	18.1 ± 1.0
YY1-5	42.6	3.3	1.8	0.7	13.8	16.1	17.6	33.6 ± 1.8
WL-1	39.1	2.4	1.4	0.6	4.2	63.6	19.2	37.5 ± 2.0
WL-2	44.0	2.9	1.9	0.7	4.2	54.6	17.0	47.0 ± 2.5
WL-3	38.8	9.0	1.1	0.6	42.1	103.0	66.3	39.9 ± 2.1
WL-4	38.4	1.7	1.3	0.6	3.9	28.3	10.5	48.5 ± 2.6
WL-5	36.7	0.6	0.9	0.6	2.8	34.8	11.0	17.4 ± 1.0
QJ-1	51.5	2.1	1.9	0.7	10.8	10.5	13.2	40.8 ± 2.2
QJ-2	47.7	3.9	1.9	0.7	8.9	22.9	14.3	72.1 ± 3.8
QJ-3	43.4	6.2	1.4	0.7	20.9	57.0	34.3	50.6 ± 2.6
QJ-4	51.3	18.1	3.3	0.7	45.7	40.1	55.1	84.3 ± 4.4
QJ-5	48.8	2.1	2.4	0.7	10.7	4.5	11.7	45.8 ± 2.9
LingY1-1	68.7	0.4	6.0	0.8	0.8	11.5	3.5	18.6 ± 1.0
LingY1-2	39.4	4.4	1.3	0.6	21.6	7.4	23.3	34.5 ± 1.9
LingY1-3	52.5	3.1	2.2	0.7	11.3	50.6	23.2	24.6 ± 1.3
LingY1-4	58.5	2.1	2.9	0.7	8.0	20.3	12.8	29.0 ± 1.6
LingY1-5	59.3	0.9	4.9	0.7	0.1	0.0	0.1	14.8 ± 12.9
Tt-1	72.3	7.1	6.3	0.8	42.5	85.7	62.7	26.3 ± 1.4
Tt-2	60.9	1.5	5.9	0.8	11.5	15.6	15.1	24.3 ± 1.3
Tt-3	71.8	6.0	8.9	0.8	27.5	96.0	50.0	27.9 ± 1.5
Tt-4	74.6	3.4	10.9	0.8	16.0	28.0	22.6	34.7 ± 1.8
Tt-5	69.8	1.1	8.2	0.8	5.3	17.4	9.4	27.5 ± 1.5
FT-1	56.4	34.8	4.1	0.8	22.9	50.6	34.8	41.6 ± 2.2
FT-2	55.3	15.7	4.4	0.7	8.3	31.6	15.7	22.3 ± 1.2
FT-3	72.6	17.0	8.8	0.8	14.3	11.3	17.0	23.4 ± 1.3
FT-4	61.4	5.2	6.2	0.8	0.0	22.0	5.2	12.1 ± 0.7
FT-5	56.8	3.9	4.3	0.7	0.8	13.3	3.9	28.3 ± 1.6
YF1-2-1	75.9	1.5	11.0	0.8	15.9	43.1	26.0	13.3 ± 0.7
YF1-2-2	58.1	0.7	4.4	0.8	4.4	59.0	18.2	9.1 ± 0.5
YF1-2-3	50.7	0.5	2.9	0.7	5.4	28.6	12.1	11.5 ± 0.6
YF1-2-4	45.9	7.1	1.9	0.6	109.0	200.3	156.0	12.1 ± 0.6
YF1-2-5	51.0	0.7	2.6	0.7	13.9	13.7	17.2	11.0 ± 0.6
YF1-2-6	56.1	0.2	4.4	0.7	1.6	18.5	6.0	9.5 ± 0.5
YF1-2-7	40.0	0.3	1.6	0.7	5.2	28.7	11.9	7.8 ± 0.6
YF1-2-8	33.6	0.6	1.1	0.6	10.4	44.9	20.9	9.5 ± 0.5
YF1-2-9	40.1	0.7	1.6	0.7	6.3	48.8	17.8	10.4 ± 0.6

Ft: alpha correction factor (Farley et al., 1996); eU: effect uranium concentration, calculated from the contents of U and Th, eU = U+0.235Th (Flowers et al., 2007).

The AHe and ZHe data are presented in Tables 2 and 3. The single grain AHe/ZHe ages are always characterized by obvious dispersion, which could be caused by various factors, including U- and/or Th-rich microinclusions (Vermeesch et al., 2007), grain size (Reiners and Farley, 2001), radiation damage (Green et al., 2006; Shuster et al., 2006) and helium implantation from an external source (Spiegel et al., 2009). The effective uranium (eU) can be used as a proxy of the degree of radiation damage (Flowers et al., 2007). There is no clear relationship between the ZHe and AHe single-grain ages and the grain size (Fig. 6b, d). The positive correlation between the AHe ages and the eU (Fig. 6a) and the negative correlation between the ZHe ages and the eU (Fig. 6c) suggest that radiation damage caused the dispersion of the ZHe and AHe single-grain ages. Grains YF1-2-4, WL-3, CSZH-1, and QJ-2 have high eU values and old ages. This may be caused by U and/or Th-rich micro--inclusions, rather than radiation damage. In addition to eU, excess He is another key factor causing ZHe age variation. The ^{4}He value is extremely high and the eU is relatively low in grains XD-3 and FT-1, suggesting significant parentless ^{4}He. The measured AHe single grain ages range from 7.8 ± 0.6 to 50.6 ± 2.6 Ma, reflecting the response to the Himalayan movement. The ZHe grain ages of samples YF1 and JS1 are significantly younger than their depositional ages, which indicates that the ZHe ages have been completely reset. The maximum paleotemperatures of samples YF1 and JS1 exceed the closure temperature of ZHe (~200 °C). With high ^{4}He value of 20.1–47.0 nmol■g^{-1}, the ZHe grain ages of sample FT are generally younger than depositional ages, whereas the grain FT-d possesses older ZHe age, which represents the thermal information of provenance area. Therefore, we infer that the ZHe grain ages have mostly been reset, and the maximum paleotemperature of sample FT is lower than the closure temperature of ZHe. The ZHe grain ages of samples WL and QJ are generally older than their depositional ages, except for grains WL-d, QJ-b, and QJ-c. All of the grains have extremely high ^{4}He contents, with values of 13.4–95.6 nmol■g^{-1}. Thus, the ZHe ages of the Jurassic samples were only partially reset, and most of the thermal information about the provenance area has been retained. The maximum paleotemperatures of samples WL and QJ are close to the ZHe partial annealing zone.

4.1.2. *Thermal histories modeling*

The thermal histories were inverted using the HeFTy software (Ketcham, 2005) and the Monte Carlo approach. Here, the parallel curvilinear model and the multi-kinetic annealing model proposed by Yamada et al. (2007) and Ketcham et al. (2007) were selected for the ZFT and AFT, respectively. The radiation damage accumulation and annealing models developed by Flowers et al. (2009) and Guenthner et al. (2013) were selected for the AHe and ZHe, respectively. In our model, 150–1000 thermal paths were developed and the best-fit

Table 3
The measured ZHe ages.

Sample	Radius (μm)	^{4}He (nmol▪g^{-1})	Mass (μg)	FT	U (ppm)	Th (ppm)	eU (ppm)	Corrected age (±1σ) (Ma)
WL-a	56.8	65.5	3.7	0.8	430.9	228.6	484.6	289.6 ± 18.0
WL-b	52.5	36.9	3.1	0.7	269.0	242.5	325.9	288.6 ± 17.9
WL-d	51.5	75.9	4.9	0.8	774.5	382.3	864.3	144.7 ± 9.0
WL-e	53.7	95.6	17.6	0.9	196.3	120.4	224.6	195.4 ± 12.1
QJ-a	87.7	42.6	15.6	0.8	100.2	50.1	112.0	197.2 ± 12.2
QJ-b	91.2	20.7	13.7	0.8	69.3	47.3	80.5	152.2 ± 9.4
QJ-c	86.5	42.8	12.6	0.8	173.1	61.3	187.5	147.4 ± 9.1
QJ-d	89.9	13.4	16.4	0.9	28.3	18.9	32.8	202.3 ± 12.5
QJ-e	47.3	31.0	1.8	0.7	542.3	320.0	617.5	224.2 ± 13.9
JS1-a	56.8	21.0	7.1	0.8	358.6	181.0	401.2	60.1 ± 3.7
JS1-b	52.5	9.5	5.0	0.8	374.6	162.9	412.9	37.4 ± 2.3
JS1-c	50.3	14.1	3.6	0.7	757.8	322.8	833.7	38.6 ± 2.4
JS1-d	51.5	15.1	4.4	0.7	892.2	444.8	996.7	28.1 ± 1.7
JS1-e	53.7	13.1	3.7	0.8	989.0	257.9	1049.6	27.9 ± 1.7
FT-a	61.3	47.0	9.9	0.8	202.7	125.0	232.0	165.2 ± 10.2
FT-b	66.1	22.9	10.1	0.8	108.4	90.0	129.5	141.8 ± 8.8
FT-c	54.9	20.1	6.1	0.8	116.2	68.9	132.4	200.0 ± 12.4
FT-d	52.2	55.3	4.3	0.7	346.3	145.0	380.4	273.1 ± 16.9
FT-a	74.7	84.1	13.5	0.8	253.1	135.6	285.0	177.6 ± 11.0
YF1-a	59.2	1.7	5.5	0.8	92.3	205.4	140.6	17.9 ± 1.1
YF1-b	59.4	18.0	5.6	0.8	227.6	50.2	239.4	109.1 ± 6.8
YF1-c	46.2	29.8	3.6	0.7	448.2	180.3	490.5	135.5 ± 8.2
YF1-d	49.8	8.9	4.0	0.7	614.3	254.8	674.2	27.3 ± 1.7
YF1-e	61.1	13.3	6.2	0.8	223.8	14.1	227.1	76.5 ± 4.7
YF1-f	42.0	1.3	2.8	0.7	97.8	85.4	117.9	32.4 ± 2.0
YF1-g	39.7	1.1	2.8	0.7	202.6	119.3	230.6	14.6 ± 0.9

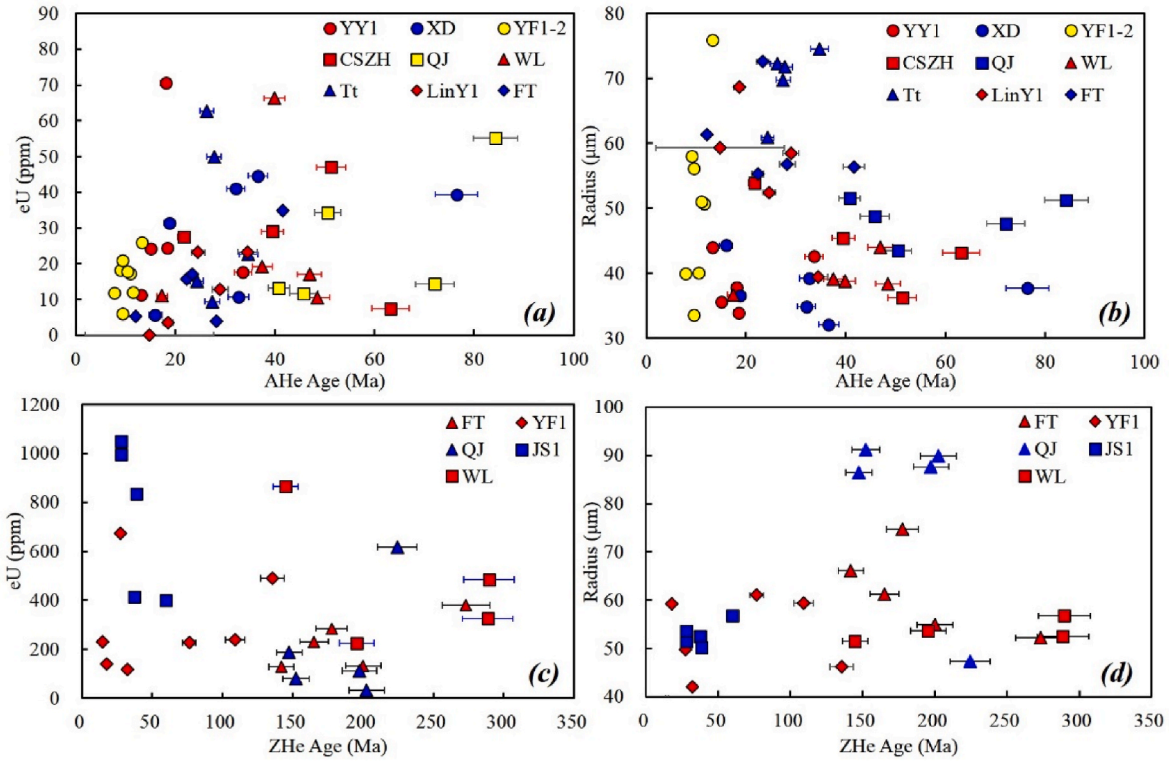

Fig. 6. (a) Correlation of AHe single grain age with eU. (b) Correlation of AHe single grain age with radius. (c) Correlation of ZHe single grain age with eU. (d) Correlation of ZHe single grain age with radius.

time-temperature (t-T) paths represent the thermal histories of the samples. It should be noted that the maximum paleotemperatures of samples JY8 and YF1-2 exceeded the AFT partial annealing zone. Owing to the fact that wells JY8 and JS1 are both located in the Jiaoshiba anticline, which is controlled by the Qiyueshan Fault, and their exposed horizon and drilled strata are similar, the thermal history of sample JY8 was constrained by that of sample JS1. In addition, the thermal history of sample YF1-2 was constrained by that of sample YF1 because these two samples are both from well YF1.

The inversion modeling results are shown in Fig. 7 and Table 4. Samples QJ and WL from the Hubei–Hunan–Guizhou fold belt cooled rapidly during the Early-Late Cretaceous, with cooling rates of 2.80 °C/Ma and 2.25 °C/Ma, respectively. Since these Late Cretaceous, the samples have cooled slowly with cooling rates of 0.69 °C/Ma and

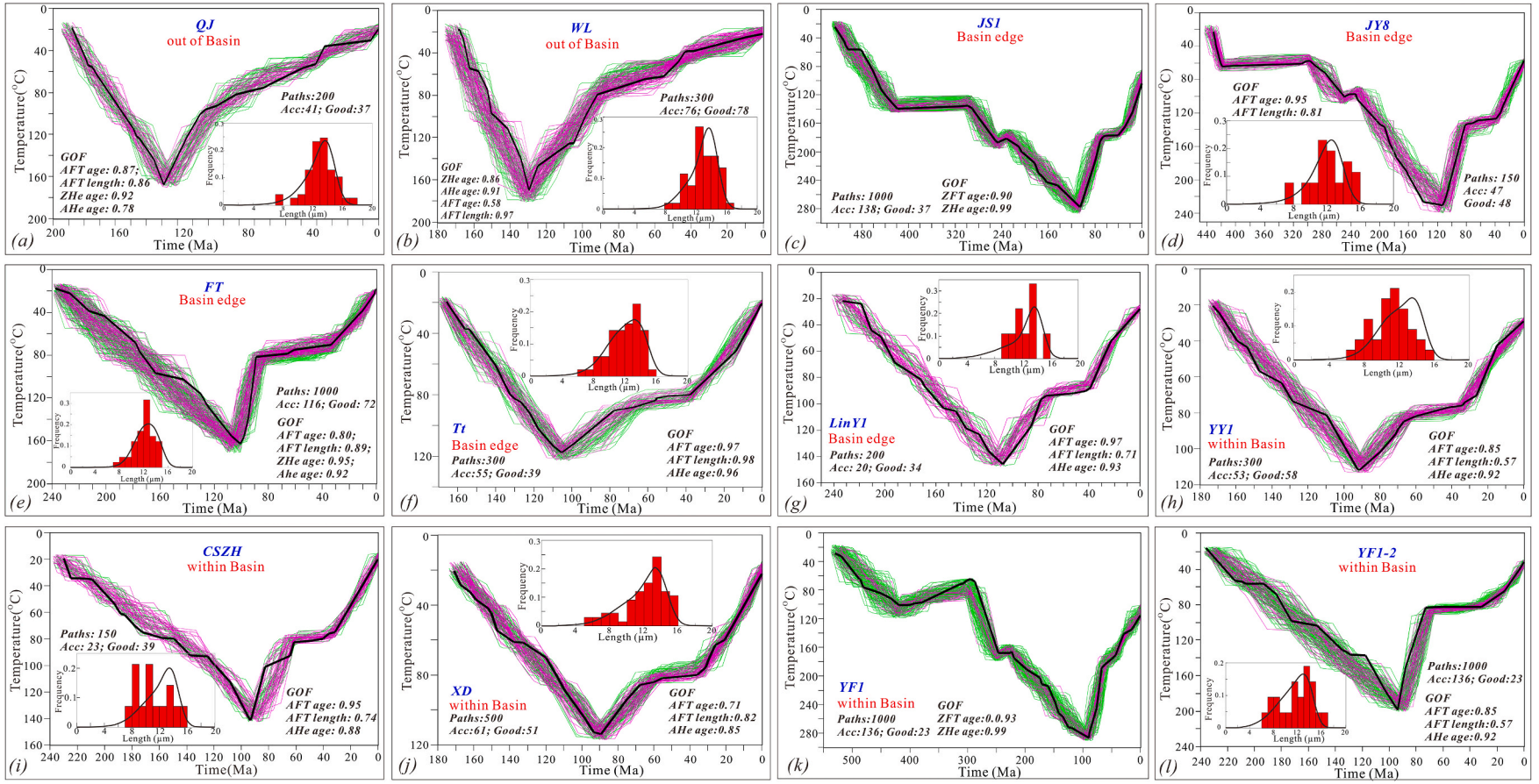

Fig. 7. Thermal inversion results reconstructed by AFT, ZFT AHe and ZHe. GOF = goodness of fit. Green lines, magenta lines and black lines represent the acceptable fit paths (GOF >0.05), good fit paths (GOF >0.5). and the best time-temperature paths, respectively. (For interpretation of the references to colour in this figure legend, the reader is referred to the Web version of this article.)

Table 4
The cooling and uplift process of samples based on HeFTy modeling results.

Sample	Duration time, Ma	Temperature Decrease, °C	Cooling rate, °C/Ma	Geothermal gradient, °C/km	Denudation, m
QJ	140–115	170–100	2.80	31	2260
	115–0	100–20	0.69		2580
WL	130–90	170–80	2.25	31	2900
	90–0	80–20	0.67		1940
JS1	110–70	280–180	2.50	31	3230
	70–40	180–175	0.17		160
	40–0	175–105	1.75		2260
JY8	110–80	230–135	3.17	32	2970
	80–40	135–125	0.25		310
	40–0	125–60	1.63		2030
FT	100–90	160–80	8.00	31	2580
	90–35	80–70	0.18		320
	35–0	70–20	1.43		1610
Tt	105–75	120–90	1.00	29	1030
	75–40	90–80	0.28		340
	40–0	80–20	1.50		2070
LinY1	110–75	145–95	1.43	31	1610
	75–40	95–90	0.14		160
	40–0	90–30	1.50		1940
YY1	90–65	110–85	1.00	34	740
	65–35	85–75	0.33		290
	35–0	75–30	1.28		1320
CSZH	93–65	140–80	2.14	34	1760
	65–35	80–75	0.17		150
	35–0	75–20	1.57		1620
XD	90–60	110–82	0.93	34	820
	60–35	82–77	0.20		150
	35–0	77–20	1.34		1680
YF1-2	95–70	200–90	4.40	33	3330
	70–35	90–85	0.14		150
	35–0	85–35	1.43		1520
YF1	92–67	275–185	3.80	33	2730
	67–40	185–170	0.56		450
	40–0	170–115	1.37		1670

0.67 °C/Ma, respectively. The cooling histories of the samples from the Sichuan Basin exhibit a periodic pattern of rapid-slow-rapid. During the Early-Late Cretaceous, these samples experienced the first phase of rapid cooling at rates of ~0.93–4.40 °C/Ma. Then, they underwent slow cooling from the Late Cretaceous to the Late Eocene at rates of 0.14–0.56 °C/Ma, followed by a final accelerated cooling stage at rates of 1.28–1.75 °C/Ma. The rapid cooling phase during the Cretaceous represents significant progressive northwestward deformation. Samples QJ and WL reached their maximum paleo-temperatures at 140 Ma and 130 Ma, respectively, while the samples from the Qiyueshan area (JS1, JY8, FT, Tt, and LinY1) reached their maximum paleo-temperatures at 105–110 Ma, and the samples from the Sichuan Basin (YY1, CSZH, YF1, YF1-2, and XD) reached their maximum paleo-temperatures at 90–95 Ma.

4.1.3. Meso-Cenozoic uplift process

The exhumation (h, m) can be restored based on the paleo-geothermal gradients (G, ∘C/km) and the best-fit time–temperature paths using following the equation:

$$h = \frac{\Delta T}{G}, \quad (2)$$

where ΔT is the temperature difference caused by uplift (∘C). In this study, the maximum paleo-geothermal gradients of typical wells are restored based on the maximum temperatures of a series of samples (Ro) at different depths. The R_{equ} data are shown in Fig. 8a and b and the maximum paleotemperature profiles (Fig. 8c and d) were reconstructed using the R_{equ} data and the EASY%R_o model (Sweeney and Burnham, 1990). The results reveal that the maximum paleo-geothermal gradient in wells JS1, JY8, and JY1 was 30 °C/km; in wells DY2 and DY5, it was 29 °C/km; in wells DY1, LY1, and NY1, it was 31 °C/km; in the well YF1, it was 33 °C/km; and in wells YY1, YY7, WY23-1, and WY35-1, it was 34 °C/km. Here, the geothermal gradients of the outcrop samples are constrained by the nearby wells. We calculated the denudation of samples QJ and WL using G_{JS1}, that of sample FT using G_{DY1}, that of Tt using G_{DY5}, that of sample CSZH using G_{YY7}, and that of sample XD using $G_{WY23\text{-}1}$. The results are presented in Table 4. By comparing the uplift processes of the samples, the differences in the Meso-Cenozoic uplift in the Hubei–Hunan–Guizhou fold belt and the Sichuan Basin were determined. The Hubei–Hunan–Guizhou fold belt underwent a two-stage uplift process characterized by rapid uplift during the Early-Late Cretaceous and then slow uplift. The Meso-Cenozoic uplift in the Sichuan Basin was rapid during the Early-Late Cretaceous, slow from the Late Cretaceous to the Late Eocene, and rapid uplift until the present.

4.2. Pressure evolution

Confined by the trapping pressures of fluid inclusions and present DFIT measured pressures, the entire pressure evolution of the Lower Silurian could be simulated. The trapping pressure of CH_4 inclusions in the Silurian shale are presented in Table 5. In this study, the burial history of the Lower Silurian strata was simulated using BasinMod 1D. The thickness, top depth, and average lithologies of the strata in the wells were provided by the Sinopec Exploration Company. The heat flow and thermal conductivity data were obtained from previous studies (Xu et al., 2011, 2018; Liu et al., 2018; Feng et al., 2021; Qiu et al., 2021). The erosion data during the Caledonian and Indosinian movements were obtained from Xu et al. (2018) and Qiu et al. (2021). The uplift processes during the Yanshanian and Himalayan movements are represented by our new results (Fig. 7, Table 4). It should be noted that the strata in well YY7 were significantly affected by the Mesozoic slip deformation. Therefore, we reconstructed the burial history of the Lower Silurian strata in this well using the thickness and top depth of the strata in adjacent well YY1, which were constrained by the uplift processes of sample CSZH. Then, the temperature and pressure evolutions were analyzed based on the fluid inclusion data and R_{equ} data. Here, the process of reconstructing the pressure evolution of the Lower Silurian strata is summarized by taking typical well YY1 as an example. Well YY1 is located in the Yongchuan area, southeastern Sichuan Basin. The Lower Silurian shale underwent three main periods of uplift, at the end of the Early Paleozoic, in the Middle-Late Triassic, and during the Cretaceous to present. Based on the R_{equ} data (Fig. 8) and the Meso-Cenozoic uplift processes, the burial and temperature evolutions were reconstructed (Fig. 9a). The R_o from Triassic and Permian and R_{equ} form Silurain are in good agreement with the simulation results (Fig. 9b). Constrained by the inclusions' pressures and the present pressure, the pressure evolution of the Lower Silurian strata was simulated (Fig. 9c). The overpressure began in the Early Triassic and increased rapidly during the Middle Jurassic. The pressure reached the maximum at 90 Ma (~116.0 MPa), followed by a rapid decrease. Currently, some of the overpressure is still retained, with pressure coefficients of 1.85.

The CH_4 inclusions data are obtained from the Sinopec Wuxi Research Institute of Petroleum Geology. *0.24–0.27 represents the range of density. 0.25 represents the average of density. **79.2–101.9 represents the range of trapping pressure. 89.0 represents the average of trapping pressure, calculated by the average of density. The trapping time and paleo-depth are calculated by the average of trapping pressure.

The pressure evolutions of the Lower Silurian strata in 12 wells were reconstructed, including wells PY1, LY1, JY1, JY8, NY1, DY1, DY4, LinY1, YY1, YY7, WY23-1, and YF1 (Fig. 10). The measured drilling pressure data (drilling stem test- DFIT) were provided by the Sinopec Exploration Company. The trapping pressure and time data of the inclusions in the samples from well DY1 were obtained from Qiu et al. (2020). The modeled pressure evolution for well YY7 is inconsistent with the trapping pressure of the inclusions, with a difference of >32 MPa in 77 Ma. This suggests that in addition to uplift, more than 32 MPa of depressurization occurred due to other mechanisms during the Early

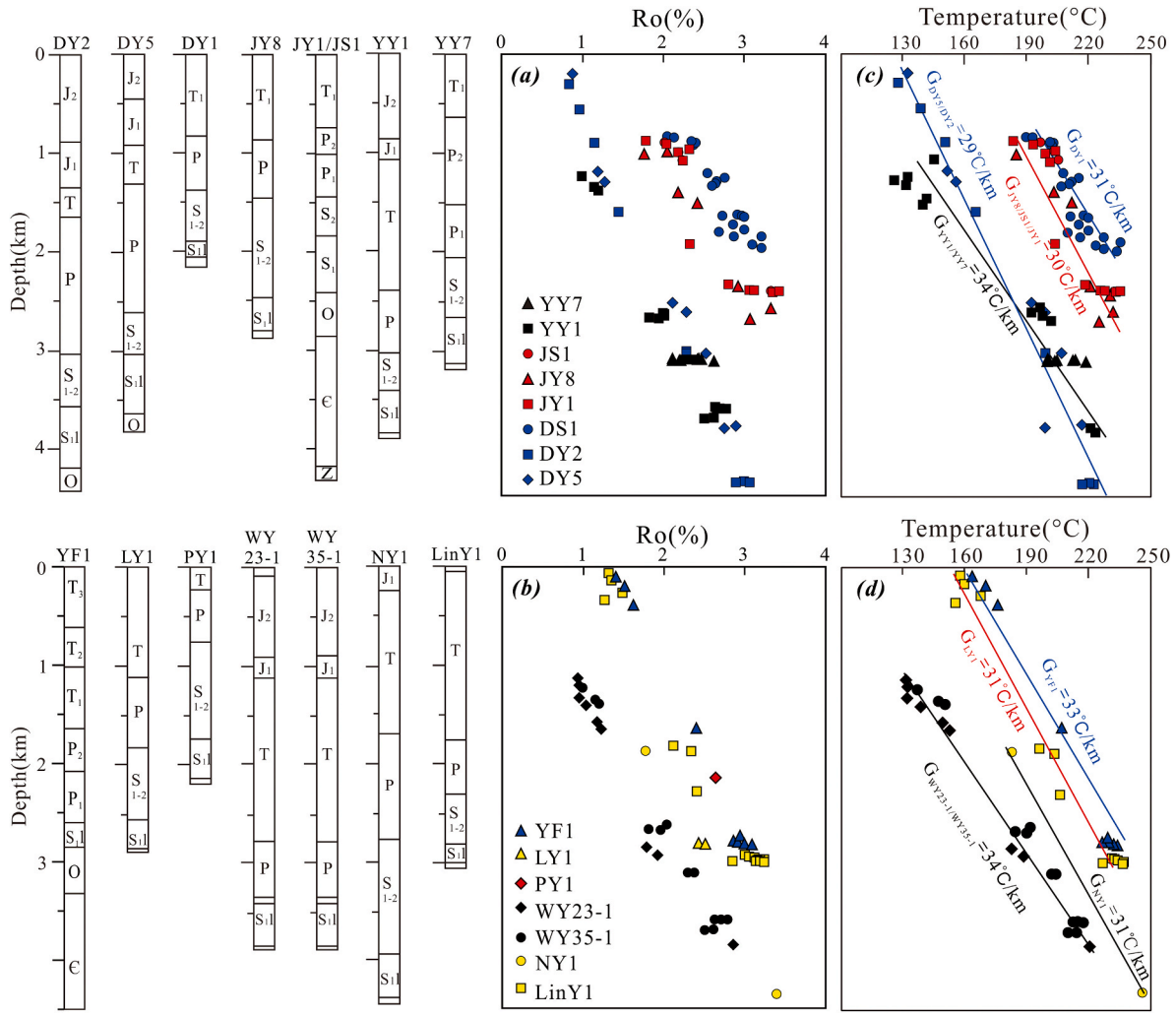

Fig. 8. (a) R_o data of 15 wells in the Upper Yangtze Block; (b) Maximum paleotemperature profiles reconstructed for 13 wells in the Upper Yangtze Block.

Table 5
The trapping pressure of CH_4 inclusions in the Silurian shale.

Sample	Depth, m	Occurrence	Raman shift, cm^{-1}	Number of CH_4 inclusion	Density, g/cm^3	Trapping temperature, °C	Trapping pressure, MPa	Trapping Time, Ma	Paleo-depth, m
YY1	3830.3	quartz	2911.65~2912.18	11	0.24–0.27 (0.25) *	170.1	79.2–101.9 (89.0) **	27	4940
YY7	3135.1	calcite	2912.80~2913.50	10	0.20–0.23 (0.21)	183.5	60.2–78.3 (66.3)	77	5597
PY1	2134.65	calcite	2914.25~2914.79	4	0.15–0.18 (0.16)	128.5	32.7–43.2 (36.8)	93	4360
NY1	4408.28	calcite	2911.74~2912.20	4	0.27–0.29 (0.28)	177.8	114.7–123.7 (118.1)	84	7022
		quartz	2911.52~2912.29	11	0.28–0.30 (0.29)	214.4	125.3–152.9 (141.8)	99	7963
JY1	2405	quartz	291,178~2912.14	12	0.27–0.28 (0.28)	215.8	122.7–132.2 126.9	101	6897
DY4	3815.5	quartz	2911.10~2912.65	6	0.24–0.27 (0.25)	150.0	73.9–98.4 (84.9)	30	5086

Cretaceous. This phenomenon will be discussed in Section 5.2.1. Except for well YY7, we also determined the excess pressure evolutions of the Lower Silurian strata in the other 11 wells (Fig. 11). The evolution results show that during the Early Triassic, rapid hydrocarbon generation occurred in the shale and overpressure began to form. The excess pressure significantly increased because the strata rapidly subsided, and the major shale gas was generated from the Middle Jurassic to the Early Cretaceous. At the end of the Early Cretaceous, the overpressure reached the maximum, ranging from 106.0 MPa to 145.0 MPa. The excess pressure in wells PY1, YY1, LingY1, DY1, and DY5 is relatively low (38.5–49.0 MPa), while the excess pressure in other wells ranges from 60.0 to 69.5 MPa. Then, the Meso-Cenozoic differential uplift process resulted in obvious differences in the pressure decrease. The pressure in well PY1 decreased normally in the Late Cretaceous (66 Ma), while that in well DY1 decreased normally in the Oligocene (~30 Ma). There was less pressure reduction in wells WY23-1 and YY1 and ultrahigh pressures

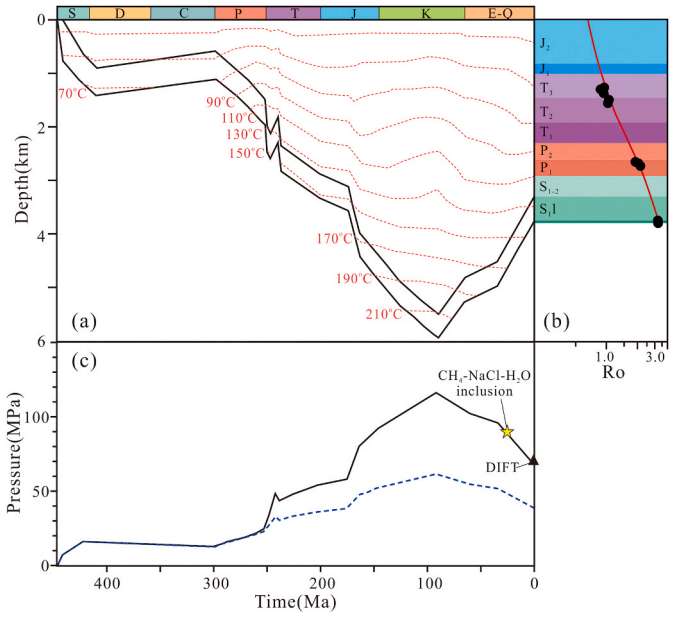

Fig. 9. (a) Burial and thermal histories for the Lower Silurian strata in well YY1. The red dashed lines represent the temperature; (b) Ro profile of well YY1. The circles in the right represent the measured Ro data; and the black line in the right represents the simulation values (Sweeney and Burnham, 1990). (c) The pressure evolution of the Lower Silurian strata. The star represents the pressure and time data for the CH_4 inclusions. The filled triangles are the measured drilling data (drilling stem test- DFIT). The black line represents the formation pressure, and the blue dashed line represents the hydrostatic pressure. (For interpretation of the references to colour in this figure legend, the reader is referred to the Web version of this article.)

are still retained, with excess pressures of >20 MPa. The other wells retained little overpressure, ranging from 5 MPa to 15 MPa.

4.3. Burial-hydrocarbon generation-uplift-gas loss evolution of shale

The temperature and pressure evolutions allow us to estimate the shale gas content during the uplift process following the method proposed by Yu et al. (2016):

(1) the adsorbed gas content was calculated:

$$V_0 = 0.3725\omega(TOC) + 1.7375, \tag{3}$$

$$P_0 = -0.3273\omega(TOC) + 3.0022, \tag{4}$$

P_0 : Langmuir pressure (MPa) in 30 °C;

$$V_L/V_0 = -0.506\left(\frac{T - T_0}{T_0}\right) + 0.9952, \tag{5}$$

T: temperature (°C); V_L: Langmuir volume (m^3/t) in T;

$$P_L/P_0 = -0.506\left(\frac{T - T_0}{T_0}\right) + 0.9952, \tag{6}$$

T: temperature (°C); P_L: Langmuir pressure in T;

$$A_g = V_L/2, \tag{7}$$

V_0: Langmuir volume (m^3/t) in 30 °C (303 K); TOC: total organic carbon content (%); A_g: adsorbed gas content (m^3/t);

(2) free gas volume was calculated:

$$V_f = \frac{1}{\rho_e} \times V_t S_g - V_a, \tag{8}$$

$$V_a = \frac{A_g}{\rho_g}, \tag{9}$$

V_f: free gas volume; V_t: porosity, %; S_g: gas saturation, %; V_a: adsorbed gas volume; ρ_g: adsorbed gas density, 0.421 g/cm^3; ρ_e: matrix density, g/cm^3

(3) free gas density was calculated using the Peng-Robinson (PR) equation (Peng and Robinson, 1976):

$$P = \frac{RT}{\rho_f - b} - \frac{a(T)}{\rho_f{}^2 + 2b\rho_f - b^2}, \tag{10}$$

$$a(T) = \frac{0.45724R^2T_C^2}{P_C}\left[1 + f(w) \times \left(1 - \sqrt{\frac{T}{T_C}}\right)\right]^2, \tag{11}$$

$$b = \frac{0.0778RT_C}{P_C}, \tag{12}$$

$$f(w) = 0.37464 + 154226w - 0.26992w^2, \tag{13}$$

w: acentric factor, 0.0113; Tc: critical temperature of CH_4, 191 K; Pc: critical pressure of CH_4, 4.6 MPa; R: 8.314472 m^3 Pa/(K·mol); T: temperature (K); P: pressure (MPa); ρ_f: free gas density (m^3/mol).

(4) free gas content was calculated:

$$A_f = \rho_f \times V_f, \tag{14}$$

A_f : free gas content $\left(m^3/t\right)$

The TOC, V_t, S_g, and ρ_e data were obtained from the Sinopec Exploration Company. The shale gas contents during the different uplift stages are shown in Fig. 12, and the results are consistent with the actual exploration data. Because the modeled pressure evolution in well YY7 is inconsistent with the trapping pressure of the inclusions, we only calculated the shale gas content in the Early Cretaceous (~93 Ma) at present. Based on the burial history, maturity, temperature, pressure, and gas content, the burial-hydrocarbon generation-erosion evolution of the Lower Silurian shale was reconstructed (Fig. 12). The shale experienced rapid subsidence during the Middle-Late Silurian and continuous uplift from the Devonian to Carboniferous. During this period, the shale had shallow burial depths, and it was always in the low maturity stage. After the Early Permian, the shale matured rapidly due to rapid subsidence, and the maturity, the shale gas content, and the pressure reached the maximum in the Early Cretaceous. Owing to the differential uplift since the Early Cretaceous, there were obvious differences in the pressure decrease process and shale gas loss. Generally, the amount of shale gas loss decreases from the Hubei–Hunan–Guizhou fold belt to the Sichuan Basin. In addition, the northwestward decrease in the coupling of the shale gas loss and the uplift amplitude indicates that the tectonic uplift controlled the shale gas preservation.

4.4. Triaxial fracturing results

Fig. 4b shows the tress–strain curves of the shale samples during the unloading process. The stress-strain curves of the shale samples during the rapid unloading process show the time it took for the shale to fracture at maximum burial depths of 5000 m, 4000 m, and 3000 m was 11.45 min, 8.40 min, and 8.36 min, respectively. Triaxial fracture tests of the shale samples during the slow unloading process show the time it took for the shale to fracture at maximum burial depths of 5000 m, 4000 m, and 3000 m was 32.47 min, 25.85 min, and 23.17 min, respectively. The results indicate that a high confining pressure increased the radial and axial plastic stages before the sample broke, making it more difficult to fracture the shale, while the unloading process for a long time has a low deviatoric stress to rock rupture and shale breaks more easily.

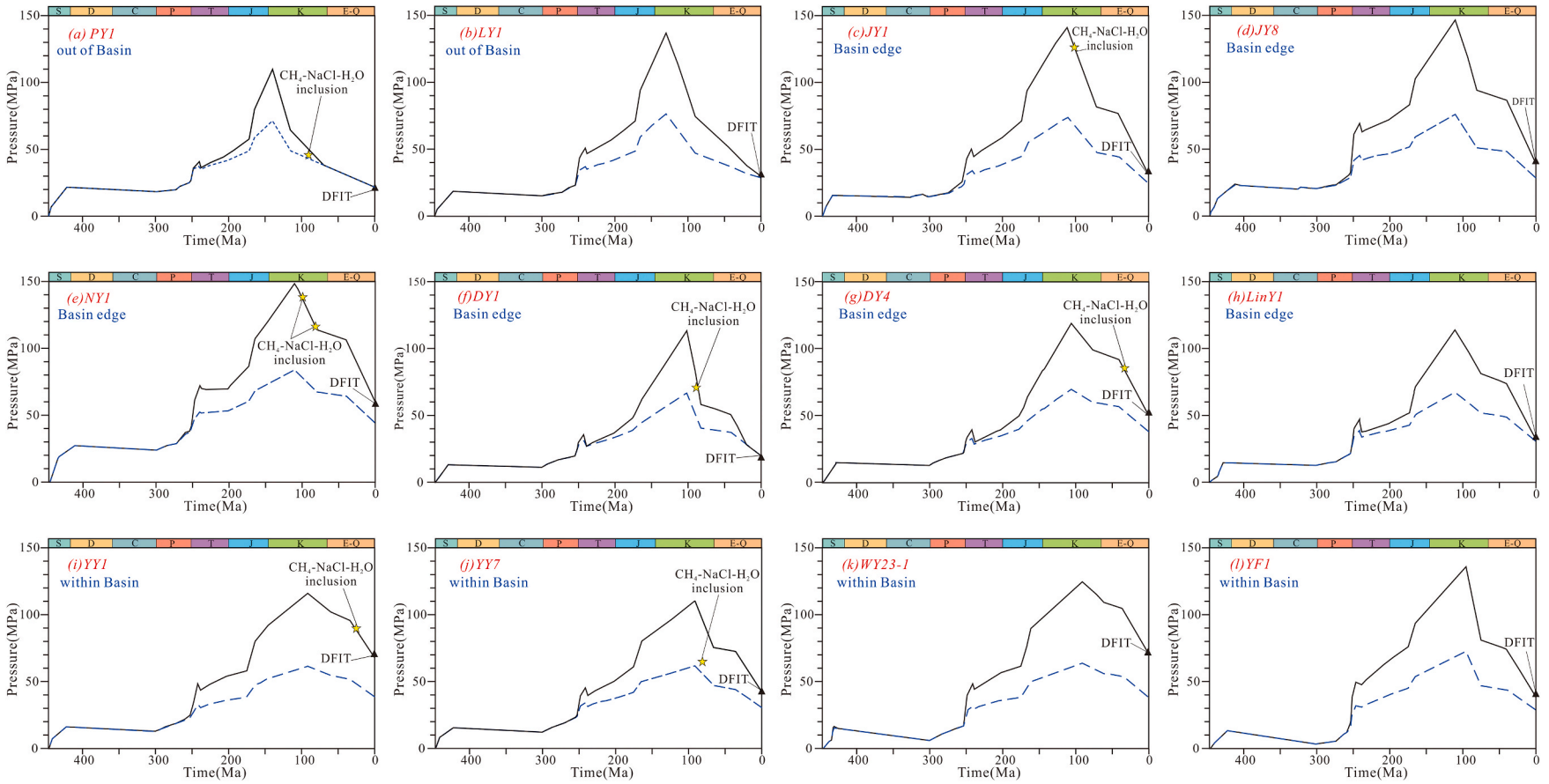

Fig. 10. The pressure evolution of the Lower Silurian strata in typical wells in the Upper Yangtze Block. The stars represent the pressure and time data for the CH_4 inclusions. The black line represents the formation pressure, and the blue dashed line represents the hydrostatic pressure. The inclusion data for well DY1 were obtained from Qiu et al. (2020), and the trapping pressure was calculated based on the method of Zhang and Frantz (1987). The filled triangles are the measured drilling pressure data (drilling stem test- DFIT) obtained from the Sinopec Exploration Company. (For interpretation of the references to colour in this figure legend, the reader is referred to the Web version of this article.)

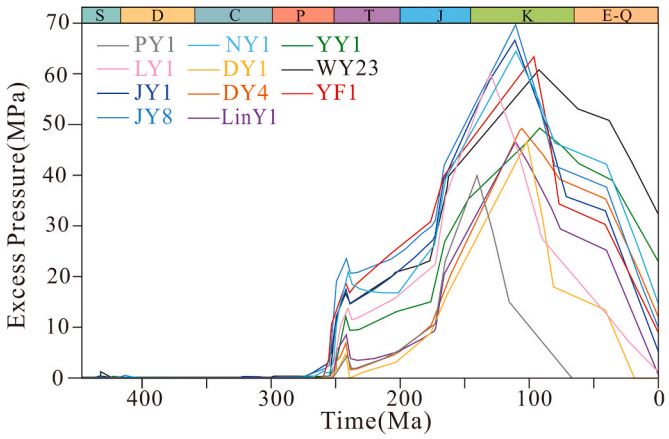

Fig. 11. The excess pressure evolution in the Lower Silurian of typical wells in the Upper Yangtze Block.

5. Discussion

5.1. Dynamic mechanism of cenozoic uplift

The Pacific-Eurasian extrusion is believed to have caused the Mesozoic regional northwestward progressive uplift in the UYB (Yan et al., 2003; Liu et al., 2005; Dong et al., 2015; Li et al., 2015). The extensional event in the South China Block, which is associated with a combination of the slab window opening during ridge subduction and rollback of the subducted Pacific slab, is connected to the decrease in the Mesozoic uplift rate (Li et al., 2014, 2017). The extensional structures in the Hubei–Hunan–Guizhou fold belt are also associated with this extensional event (Yuan et al., 2010; Sternai et al., 2014; Wang et al., 2014). The dynamic mechanism of the Cenozoic uplift is not clear. Most scholars believe that the rapid uplift since the Eocene occurred in response to the remote effect of the India-Asia collision (Richardson et al., 2008; Deng et al., 2013; Li and Shan, 2011; Tian et al., 2018; Liu et al., 2021a). However, thermochronology analysis indicates that the Wuling and Xuefeng mountains in the southern part of the UYB underwent rapid denudation after 84 Ma (Tang et al., 2014; Wang et al., 2014). As the front belt of the subduction of the Pacific Plate, the Xuefeng Mountains consistently retained the compressional background during the Late Cretaceous. Moreover, Northrup et al. (1995) and Li et al. (2014) have suggested that the rate of the Pacific-Eurasia convergence decreased from ~120 to 140 mm/yr in the Late Cretaceous to ~30–40 mm/yr in the Eocene and then increased to ~70–110 mm/yr from the Oligocene to the Early Miocene. The trend and time of these convergence rate changes are consistent with the thermal histories reconstructed using the thermochronology data for the Hubei–Hunan–Guizhou fold belt and eastern Sichuan Basin (Richardson et al., 2008; Mei et al., 2010; Shi et al., 2016; Wu et al., 2020; Liu et al., 2021a). Therefore, several studies have proposed that the Meso-Cenozoic rapid-slow-rapid uplift pattern in the eastern Sichuan fold belt was associated with the changes in the rate and direction of the Pacific-Eurasia convergence (Li et al., 2014; Wu, 2019). The Cenozoic Eurasia–Indian plate subduction and collision resulted in the uplift of the Qinghai Tibetan Plateau and lateral shearing along the Xianshuihe fault in the UYB. The Longmen Shan fault belt in the western Sichuan Basin underwent rapid uplift when it was dragged by this lateral movement (Sternai et al., 2014; Wang et al., 2014; Tian et al., 2018; Tong et al., 2019; Liu et al., 2021a). Whether or not the Eurasia–Indian collision affected the tectonic evolution of the Hubei–Hunan–Guizhou fold belt is still controversial.

Based on several low-temperature thermochronology datasets, we reconstructed the thermal histories of 12 samples, including samples WY23-1, YF1 in the central Sichuan Basin, CSZH, YY1, JS1, JY8, FT, Tt, and LingY1 from the eastern Sichuan Basin and samples WL and QJ from the Hubei–Hunan–Guizhou fold belt. Our results show that the Cenozoic uplift was characterized by inherited slow uplift in the Hubei–Hunan–Guizhou fold belt, while the Sichuan Basin has experienced rapid uplift since the Late Eocene. This difference in the uplift process indicates that the tectonic evolution of the Hubei–Hunan–Guizhou fold belt may not have been affected by the Eurasia–Indian plate subduction during the Himalayan period. The slow uplift since the Late Cretaceous was most likely associated with the Pacific-Eurasia convergence. Conversely, the rapid uplift of the Sichuan Basin since the Late Eocene was caused by the Eurasia–Indian plate subduction and collision. Moreover, the samples from the Qiyueshan area on the eastern boundary of the eastern Sichuan Basin (JS1, JY8, FT, Tt, and LingY1) indicate >2000 m of denudation since the Late Eocene, while the samples from the SCB and eastern Sichuan Basin (WY23-1, YF1 CSZH, YY1) indicate denudation of 1300 m–1600 m. The high denudation in the Qiyueshan area may be the combined result of the Eurasia–Indian collision and the Pacific-Eurasian extrusion.

5.2. Effect of tectonic reworking on shale fracturing and gas preservation

The ultralow porosity (2–8%) and low permeability (10–100 nD) characteristics determine the gas adsorption and storage mechanism inside the shale (Ougier-Simonin et al., 2016; Li et al., 2018). The occurrence states of the shale gas mainly includes free gas and adsorbed gas (Curtis, 2002; Zhu et al., 2020). As typical in-situ reservoirs, the gas content is the result of the dynamic balance between the shale gas generation, retention, and loss during the burial-uplift process. Good preservation conditions are key geological factors for shale gas accumulation (Guo et al., 2017). In this study, based on the results of the triaxial fracturing tests conducted on the Lower Silurian shale and the differences in the processes of uplift, pressure decrease, fracturing, and shale gas lose, the effect of the tectonic reworking on the shale gas preservation was determined from the perspectives of the slip deformation, uplift, and maximum burial depth.

5.2.1. Slipping deformation

The effect of the tectonic activity intensity on shale gas preservation has been analyzed based on the strength of the fault, fracture development, and structural style (Evans et al., 2014; Ferrill et al., 2014; Hu et al., 2014; Guo et al., 2017; He et al., 2019). Faults with small scales, fractures with weak intensity, and wide and gentle structural styles are conducive to shale gas preservation. It should be noted that there is a 400 km wide Mesozoic intracontinental fold-and-thrust belt in the Yangtze Block. As one of the detachments within the allochthonous succession, the Lower Silurian strata experienced obvious slip deformation in the eastern Sichuan Basin (Yan et al., 2003; Dong et al., 2015). The effect of the slip deformation on shale fracturing and gas preservation is not clear. Here, we explore it through a case study in the Yongchuan area (Fig. 1 and 13). The Yongchuan area is one of the important shale gas areas discovered in the Lower Silurian strata in the eastern Sichuan Basin. As a thrust nappe structure, the Yongchuan area is characterized by significant slip deformation (Fig. 13c). Well YY7 is located in the anticlinal core where there is obvious slip deformation of the Lower Silurian shale, while well YY1 is located in the western syncline where weak deformation of the gentle shale layer has occurred (Fig. 13a). The uplift process and pressure evolution of the Silurian strata suggest that during the Late Cretaceous (77 Ma), the uplift amplitude of the shale differed by < 1000 m, but the difference in the pressure decreases in wells YY7 and YY1 was less than 32 MPa (Fig. 10, Table 4). The actual decrease in pressure far exceeded that caused by the uplift, indicating the obvious destructive effect of the slip deformation on the pressure and gas preservation. Furthermore, the seismic coherence attribute analysis revealed that there are few fractures in the Lower Silurian shale in well YY1, while well YY7 contains significant fractures (Fig. 13b). These facts all suggest that the slip deformation played an

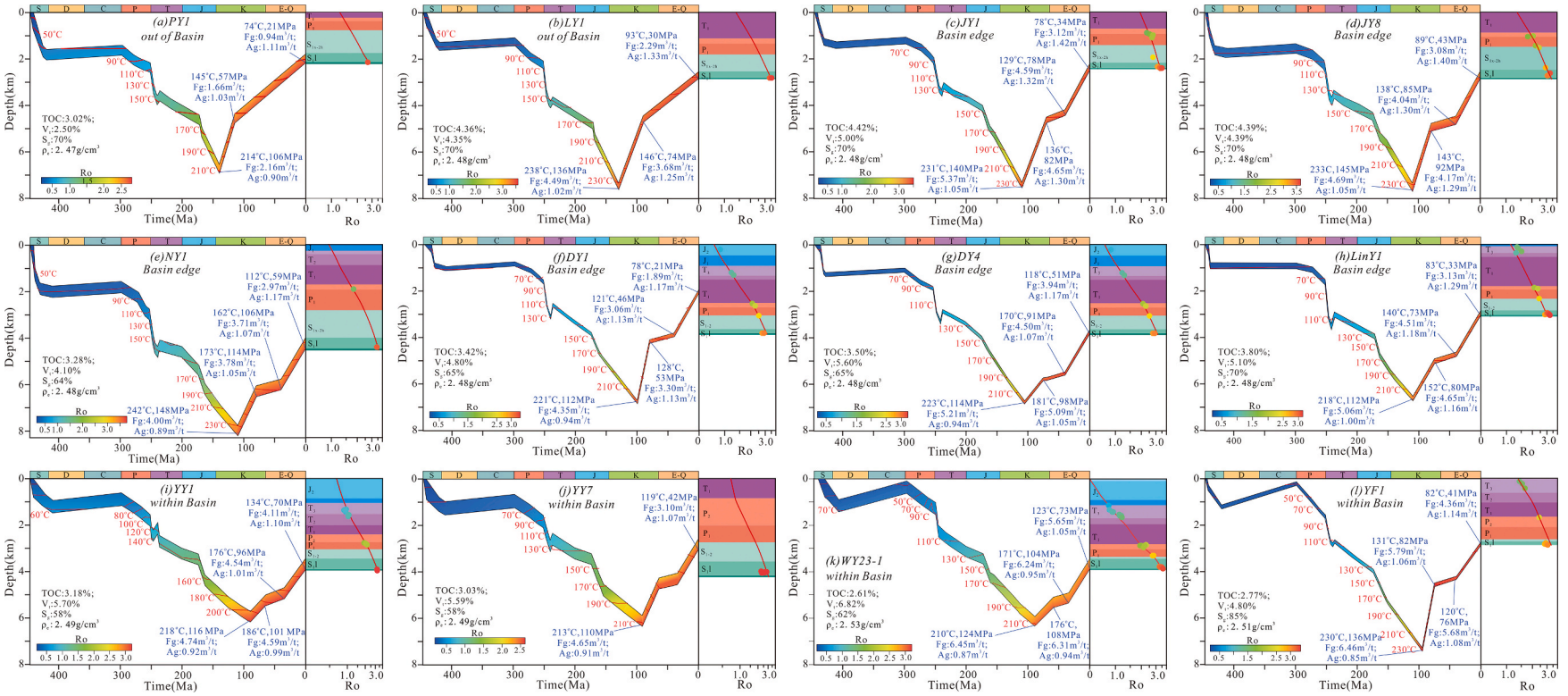

Fig. 12. The burial-hydrocarbon generation-uplift-gas loss evolution of the Lower Silurian shale. TOC: total organic carbon (%) V_t: porosity (%); S_g: gas saturation (%); ρ_e: matrix density (g/cm^3); Ag: adsorbed gas content (m^3/t); F_g: free gas content (m^3/t). The temperature, pressure, and gas content at the bottom of the Lower Silurian shale are 213 °C, 110 MPa, and 4.65 m^3/t, respectively.

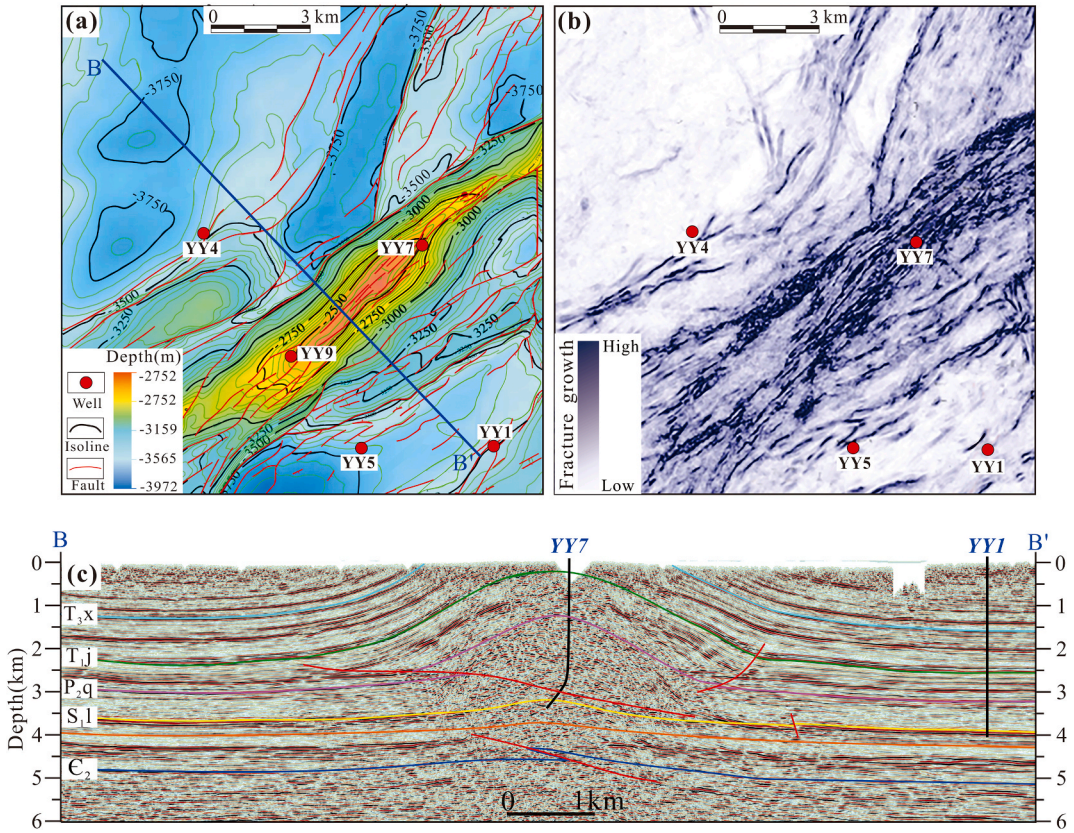

Fig. 13. (a) Geological map of the lower Silurian in the Yongchuan area; (b) The characteristics of fracture growth in the Lower Silurian shale; (c) Seismic section in Yongchuan area.

important role in the shale fracturing and gas preservation. Intensive slip deformation increased the fracture growth in the shale, resulting in a massive pressure decrease (>32 MPa) in well YY7. During the Early–Late Cretaceous, the shale in well YY1 suffered weak slip deformation and a few fractures were generated, accompanied by 15 MPa of depressurization and 0.07 m^3/t of gas diffusion.

5.2.2. *Uplift process*

Uplift is believed to increase the gas diffusion coefficient and result in depressurization (Schloemer and Krooss, 2004). During the uplift process, shale will transform into a brittle over-consolidated material, resulting in microfractures, porosity and permeability increases, and destruction of the shale's seal (Nygård et al., 2006; Guo et al., 2017; He et al., 2020; Liu et al., 2020). This study focused on the Lower Silurian shale in the Dingshan area, which has the same hydrocarbon generation characteristics and can be used to identify the effect of uplift on shale fracturing and gas preservation. The Dingshan area is located in the southeast margin of the Sichuan Basin (Fig. 1). As a thrust nappe structure controlled by the Qiyueshan Fault, the Dingshan area is characterized by significant differences in the depth of the Lower Silurian shale, exhibiting differential northwest-southeast vertical uplift (Fig. 14a, e). Furthermore, the horizontal pressure zoning in the Lower Silurian shale indicates obvious differential enrichment of shale gas due to the positive correlation between the pressure and gas content (Fig. 14b). Therefore, the Dingshan area provides an excellent opportunity to gain a better understanding of the relationship between the differential uplift and shale gas preservation. The thermal history of sample FT suggest that well DY1 began to uplift at ~100 Ma resulting in ~4500 m of denudation; while based on the thermal history of sample Tt, well DY4 was uplifted at ~110 Ma resulting in ~3450 m of denudation (Fig. 7, Table 4). During the Meso-Cenozoic, the shale gas content of well DY1 decreased from 5.50 m^3/t to 3.15 m^3/t, while the shale gas loss of well DY4 was 1.05 m^3/t (Fig. 15). The fracture growth characteristics predicted by the seismic curvature attributes show that there is a large amount of fractures in the Lower Silurian shale and roof in well DY1, while well DY4 possesses few fractures (Fig. 14c and d). The coupling due to the differential uplift, differential depressurization, and shale gas loss demonstrate that the preservation of the shale gas was controlled by the differential uplift. Under moderate uplift, there few fractures formed in the shale and roof and a small amount of shale gas diffusion occurred, while enormous uplift resulted in obvious fractures and massive shale gas dissipation. The uplift, pressure decrease, and shale gas loss processes of the Lower Silurian shale in wells JY1, JY8, and NY1 in the eastern Sichuan Basin and wells YF1 and WY23-1 in the central Sichuan Basin also indicate that the larger uplift amplitude resulted in more depressurization and shale gas loss (Fig. 15). Furthermore, the positive correlations between the uplift amplitude and the shale gas content and depressurization show that the uplift amplitude was the major factor controlling the shale gas preservation (Fig. 16a and b). The larger the uplift amplitude, the worse the preservation conditions of shale gas.

Because uplift causes hydrocarbon generation stagnation and increases the gas diffusion coefficient (Schloemer and Krooss, 2004; Liu et al., 2020), the uplift duration should play an important role in shale gas preservation, and late uplifting is favorable for shale gas preservation (Guo et al., 2017; He et al., 2020). Triaxial fracture tests (Fig. 4b) support that if the uplift process lasts for a long time, the shale breaks under a low deviatoric stress, suggesting that a long uplift duration makes shale fracturing more easily. However, the uplift duration, depressurization amplitude, and shale gas loss are not correlated, and the shale possesses similar uplift amplitudes (Fig. 16c and d), indicating that the uplift duration may not have a significant impact on the shale gas preservation and is not the is not the main controlling factor of differential shale gas preservation in the UYB. By comparing the uplift

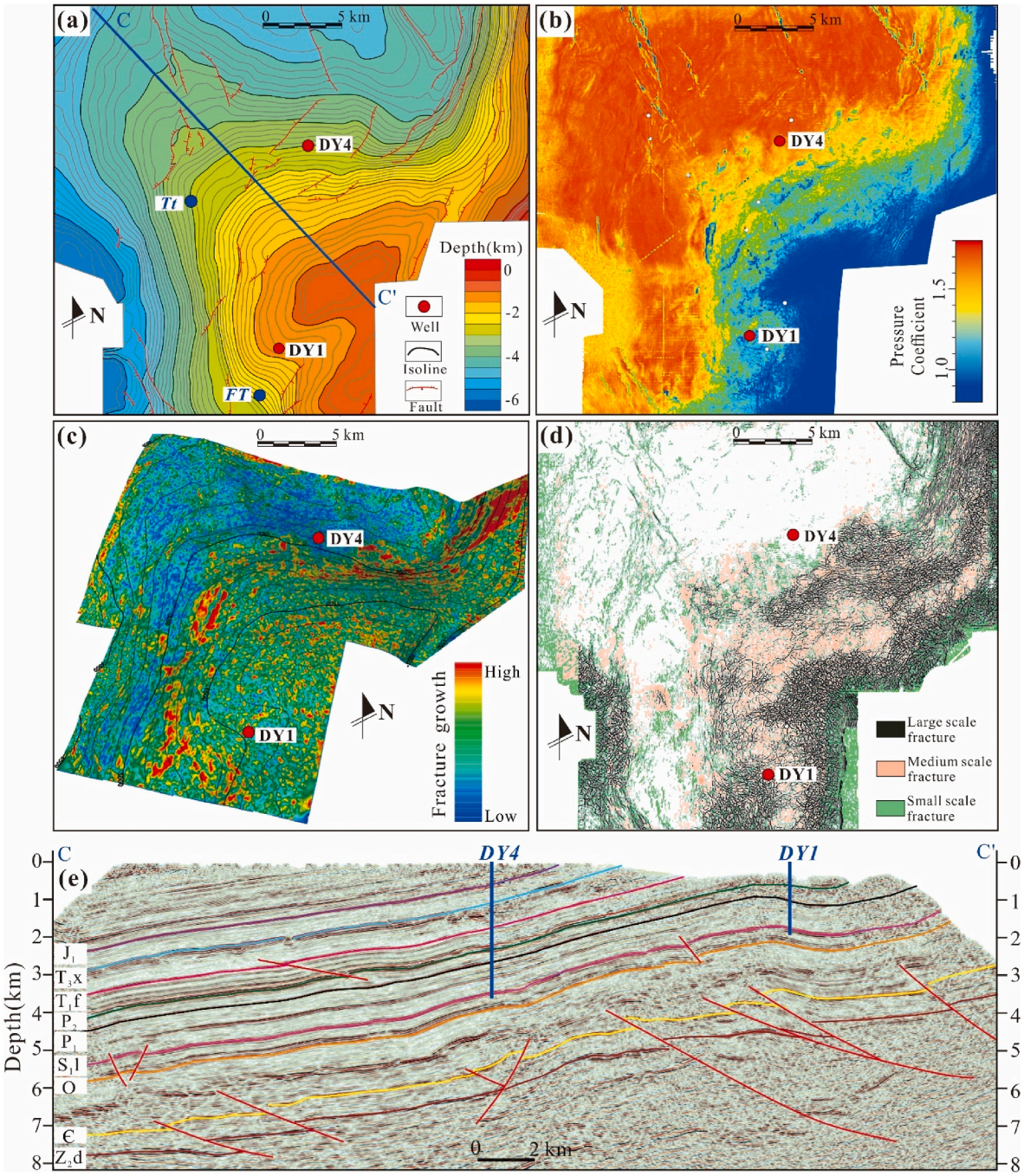

Fig. 14. (a) Geological map of the lower Silurian in the Dingshan area; (b) Pressure distribution characteristics of the Lower Silurian in the Dingshan area; (c) The characteristics of fracture growth in the Lower Silurian shale; (d)The characteristics of fracture growth in roof. The roof includes the middle Silurian green silty mudstone and the upper section of the Lower Silurian. (e)Seismic section C–C′ in Dingshan area. (For interpretation of the references to colour in this figure legend, the reader is referred to the Web version of this article.)

duration and shale gas loss processes of the Lower Silurian shale in wells DY1, LY1, and PY1, which have similar uplift amplitudes (~4720–5000 m), it was found that the uplift duration of well DY1 (~100 Ma) was shorter than that of wells LY1 and PY1 (130–140 Ma), but well DY1 experienced more shale gas loss with a value of ~2.2 m^3/t (Fig. 15). This is associated with the strain characteristics of the shale during the unloading process. The gas diffusion coefficient is low before the shale fracturing and the microfractures in the shale affect its mechanical and transport properties; however, for this to happen, they must be at least partially open. During the early uplift stage, the small amount of uplift resulted in small increases in the shale porosity and permeability, and thereby, the shale gas rarely diffused. For example, only 0.13 m^3/t of shale gas diffusion loss occurred in well WY23-1 from 90 Ma to 35 Ma (Fig. 15). Until the shale reached the brittle zone, brittle shear occurred, resulting in percolating microfractures, rapid increases in porosity and permeability, and a large amount of shale gas diffusion. Differential uplift and depressurization mainly occurred in the Late Mesozoic, and the Cenozoic was the main period of differential shale gas loss (Fig. 15). Therefore, the uplift duration after shale rupturing controls the shale gas loss. Even if the shale uplift later but reaches the rock rupture point earlier, the shale gas loss will be larger.

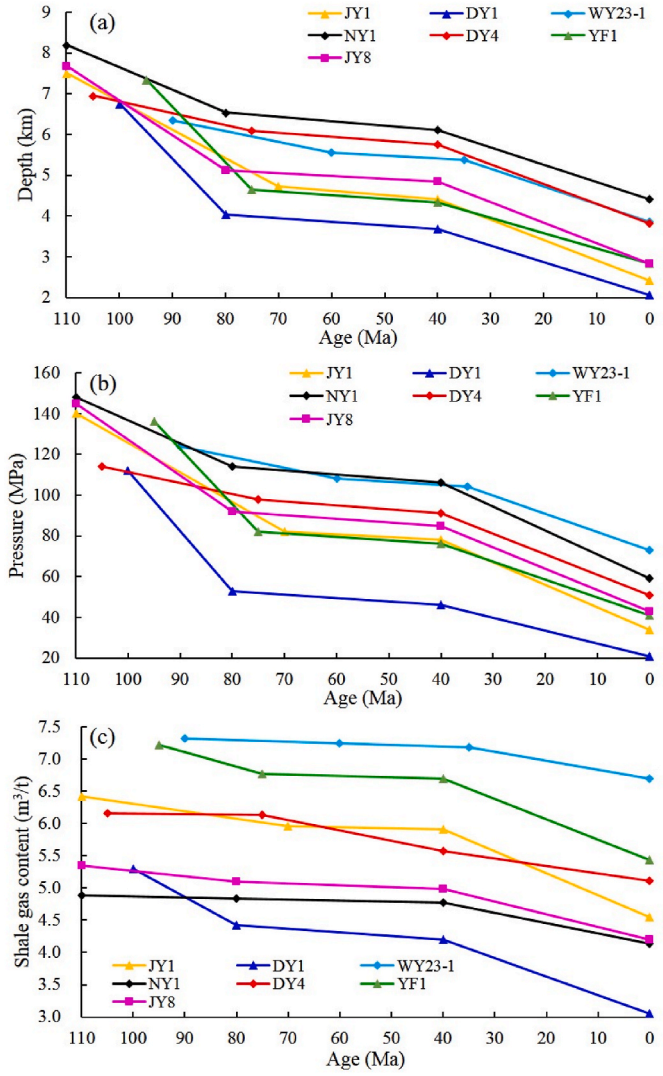

Fig. 15. Uplift (a), depressurization (b) and shale gas loss (c) processes of the Lower Silurian shale.

5.2.3. *Maximum buried depth of shale*

The maximum burial depth controls the maximum paleotemperature and pressure and plays an important role in the maturity and mechanical properties of shale. Previous studies have demonstrated that a high confining pressure increases the toughness, strength limit, and Young's modulus of shale (Masri et al., 2014; Tian et al., 2014; Chen et al., 2016; Tan et al., 2020). Triaxial fracturing tests under different confining pressures and temperatures have revealed that under a low confining pressure and temperature, elastic deformation mainly occurs before the shale brakes, while under a high confining pressure and temperature, the nonlinear deformation characteristics become obvious (Zeng et al., 2016; Tan et al., 2020). The stress–strain curves of shale during unloading (Fig. 4b) also show that a high confining pressure lengthens the radial and axial plastic stages, making the formation of shale fractures more difficult. For deeper buried shale, even though the shale has a larger uplift amplitude, there is less gas loss. Therefore, the correlation between the uplift amplitude and the shale gas loss ($R^2 = 0.89$) is better than that between the uplift amplitude and depressurization ($R^2 = 0.61$) (Fig. 16a and b). Moreover, the maximum burial depth plays an important role in the brittle deformation zone and has an indirect impact on the shale gas preservation during the uplift process. For example, the shale in wells JY1 and JY8, which have maximum burial depths of >7500 m, experienced 4800 m of uplift and shale gas loss of 1.3–1.9 m^3/t, while the maximum burial depth of the shale in well DY1 is ~6700 m and the uplift amplitude was ~4700 m, resulting in ~2.2 m^3/t of shale gas loss. The triaxial fracturing tests conducted on the Lower Silurian shale core samples from well JY2 revealed that microfractures were generated until the shale reached depths of 1000–1500 m and the confining pressure decreased from 50 MPa to 16.2 MPa. Yuan et al. (2017) proposed that the bottom boundaries of the brittle zones of the Lower Silurian shale in wells JY1 and DY1 are 2195 m and 1940 m, respectively, and the brittle–ductile transition zones are located are depths of 2195–4464 m and 1940–4492 m, respectively. The shale in wells JY1 and JY8, which have present burial depths of >2164 m, are mostly distributed in the brittle–ductile transition zone and have good sealing properties. The present burial depth of the Lower Silurian shale in well DY1 is 1894–2050 m, and the shale is mainly distributed in the brittle zone and has poor sealing properties.

6. Conclusions

The tectonic-thermal evolutions constrained by the AFT, ZFT, AHe, and ZHe analyses indicate that the UYB underwent progressive northwestward deformation with different periodic uplift during the Meso-Cenozoic. The Hubei–Hunan–Guizhou fold belt underwent a two-stage uplift process characterized by rapid uplift during the Early-Late Cretaceous and then slow uplift, while the Meso-Cenozoic uplift process in the Sichuan Basin was rapid during the Early-Late Cretaceous and slow from the Late Cretaceous to the Late Eocene, followed by rapid uplift since then. The differences in the Cenozoic uplift processes suggest that the slow uplift of the Hubei–Hunan–Guizhou fold belt since the Late Cretaceous was most likely associated with the Pacific-Eurasia convergence, while the rapid uplift of the Sichuan Basin since the Late Eocene was caused by the Eurasia–Indian plate subduction and collision. The large amount of denudation in the Qiyueshan area near the basin's eastern margin may have been due to the combined effects of the Eurasia–Indian collision and the Pacific-Eurasian extrusion.

Owing to the differential Meso-Cenozoic uplift, there were obvious differences in the pressure decrease and shale gas loss processes. The differential uplift and depressurization mostly occurred in the Late Mesozoic, while the Cenozoic was the main period of differential shale gas loss. Based on the results of the triaxial fracturing tests and the differences in the uplift, pressure decrease, fracturing, and shale gas loss of the Lower Silurian shale, the effect of the tectonic reworking on the shale gas preservation was investigated from the perspective of the slip deformation, uplift, and maximum burial depth. The differences of slip deformation, tectonic uplift amplitude and the maximum burial depth of shale resulted in the differential enrichment of the Lower Silurian shale gas. It allowed to reach the following conclusions: (1) The intensive slip deformation increased the fracture growth in the shale, resulting in a massive pressure decrease and deterioration of the shale gas preservation. (2) The uplift amplitude was the major factor controlling the shale gas preservation. Under moderate uplift, there were few fractures in the shale and roof and a small amount of shale gas diffusion occurred, while enormous uplift resulted in obvious fractures and massive shale gas dissipation. (3) Long uplift duration makes the formation of shale fractures easier. However, the uplift duration was not correlated with the depressurization amplitude and the shale gas loss, suggesting that the uplift duration has little effect on the differential enrichment of shale gas. (4) The maximum burial depth controlled the maximum paleopressure and thereby played an important role in the shear fracturing of the shale and the shale gas preservation during the uplift process. The deeper buried shale developed a higher confining pressure, lengthening the radial and axial plastic deformation stages and making shale fracturing and gas loss more difficult.

Credit author statement

Qianqian Feng: Conceptualization, Methodology, Writing - review

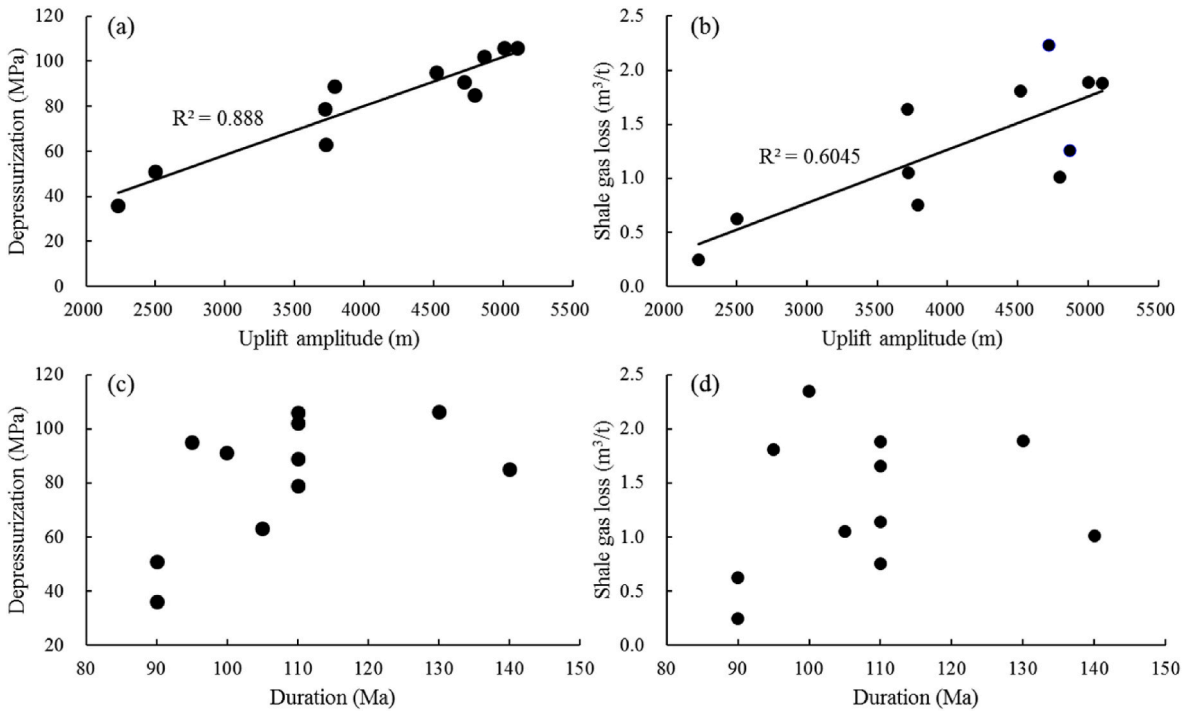

Fig. 16. (a) Correlation of uplift with depressurization; (b) Correlation of uplift with shale gas loss; (c) Correlation of uplift time with depressurization; (d) Correlation of uplift time with shale gas loss.

& editing, Resources. **Nansheng Qiu**: Conceptualization, Funding acquisition, Project administration, Supervision, Writing - review & editing. **Tenger Borjigin**: Investigation, Funding acquisition, Resources. **Fei Li**: Supervision, Resources. **Ruiyun Ji**: Validation, Writing - review & editing. **Xin Liu**: Validation, Writing - review & editing. **Yuanyuan Zhou**: Supervision, Resources, Investigation. **Aiqiang Cao**: Investigation, Formal analysis.

Declaration of competing interest

The authors declare that they have no known competing financial interests or personal relationships that could have appeared to influence the work reported in this paper.

Data availability

Data will be made available on request.

Acknowledgments

The National Natural Science Foundation of China (by projects No. 41830424, U19B6003, U2244208) provided financial support. We gratefully acknowledge the SINOPEC Exploration Company and the Wuxi Research Institute of Petroleum Geology for providing geologic information and core samples. All of the data used for this study are contained within the manuscript.

Appendix A. Supplementary data

Supplementary data to this article can be found online at https://doi.org/10.1016/j.marpetgeo.2022.106069.

References

Assad, G., Ralf, L., Garri, G., Christoph, H., 2018. Assessment of unconventional shale gas potential of organic-rich Mississippian and Lower Pennsylvanian sediments in western Germany. Int. J. Coal Geol. 198, 29–47. https://doi.org/10.1016/j.coal.2018.08.008.

Bernet, M., 2009. A field-based estimate of the zircon fission-track closure temperature. Chem. Geol. 259 (3–4), 181–189. https://doi.org/10.1016/j.chemgeo.2008.10.043.

Chang, J., Qiu, N.S., Liu, S., Cai, C.E., Xu, Q.C., Liu, N., 2019a. Post-Triassic multiple exhumation of the Taihang Mountains revealed via low-T thermochronology: implications for the paleo-geomorphologic reconstruction of the North China Craton. Gondwana Res. 68, 34–49. https://doi.org/10.1016/j.gr.2018.11.007.

Chang, J., Li, D., Min, K., Qiu, N.S., Xiao, Y., Wu, H., Liu, N., 2019b. Cenozoic deformation of the Kalpin fold-and-thrust belt, southern Chinese Tian Shan: new insights from low-T thermochronology and sandbox modeling. Tectonophysics 766, 416–432. https://doi.org/10.1016/j.tecto.2019.06.018.

Chen, Q., Zhang, J.C., Tang, X., Li, W.J., Li, Z.M., 2016. Relationship between pore type and pore size of marine shale: an example from the Sinian-Cambrian formation, upper Yangtze region, South China. Int. J. Coal Geol. 158, 13–28. https://doi.org/10.1016/j.coal.2016.03.001.

Cogné, N., Chew, D.M., Donelick, R.A., Ansberque, C., 2020. LA-ICP-MS apatite fission track dating: a practical zeta-based approach. Chem. Geol. 531, 119302 https://doi.org/10.1016/j.chemgeo.2019.119302.

Curtis, J.B., 2002. Fractured shale-gas systems. AAPG (Am. Assoc. Pet. Geol.) Bull. 11 (86), 1921–1938.

Deng, B., Liu, S.G., Li, Z., Jansa, L.F., Liu, S., Wang, G.Z., Sun, W., 2013. Differential exhumation at eastern margin of the Tibetan Plateau, from apatite fission-track thermochronology. Tectonophysics 591, 98–115. https://doi.org/10.1016/j.tecto.2012.11.012.

Ding, W.L., Dai, P., Zhu, D.W., Zhang, Y.Q., He, J.H., Li, A., Wang, R.Y., 2016. Fractures in continental shale reservoirs: a case study of the Upper Triassic strata in the SE Ordos Basin, Central China. Geol. Mag. 153 (4), 663–680. https://doi.org/10.1017/S001675681500062X.

Donelick, R.A., O'Sullivan, P.B., Ketcham, R.A., 2005. Apatite fission-track analysis. Rev. Mineral. Geochem. 58 (1), 49–94. https://doi.org/10.2138/rmg.2005.58.3.

Dong, S.W., Zhang, Y.Q., Gao, R., Su, J.B., Liu, M., Li, J.H., 2015. A possible buried Paleoproterozoic collisional orogen beneath central South China: evidence from seismic-reflection profiling. Precambrian Res. 264, 1–10. https://doi.org/10.1016/j.precamres.2015.04.003.

Duan, Z.H., Moller, N., Weare, H.H., 1992. An equation of state for the CH4-CO2-H2O system: I. Pure systems from 0 to 1000°C and 0 to 8000 bar. Geochem. Cosmochim. Acta 56, 2619–2631. https://doi.org/10.1016/0016-7037(92)90347-L.

Dunkl, I., 2002. Trackkey: a Windows program for calculation and graphical presentation of fission track data. Comput. Geosci. 1 (28), 3–12. https://doi.org/10.1016/S0098-3004(01)00024-3.

Evans, M.A., DeLisle, A., Leo, J., Lafonte, C.J., 2014. Deformation conditions for fracturing in the middle devonian sequence of the central appalachians during the late paleozoic alleghenian orogeny. AAPG (Am. Assoc. Pet. Geol.) Bull. 98 (11), 2263–2299. https://doi.org/10.1306/07221413135.

Farley, K.A., Wolf, R.A., Silver, L.T., 1996. The effects of long alpha-stopping distances on (U-Th)/He ages. Geochem. Cosmochim. Acta 60 (21), 4223–4229. https://doi.org/10.1016/S0016-7037(96)00193-7.

Feng, G.X., Chen, S.J., 1988. The relationship between bitumen reflectance and vitrinite reflectance in the strata. Nat. Gas. Ind. 8 (3), 20–25 (in Chinese).
Feng, Q.Q., Qiu, N.S., Fu, X.D., Li, W.Z., Xu, Q., Li, X., Wang, J.S., 2021. Permian geothermal units in the Sichuan Basin: implications for the thermal effect of the Emeishan mantle plume. Mar. Petrol. Geol. 132, 105226 https://doi.org/10.1016/j.marpetgeo.2021.105226.
Ferrill, D.A., McGinnis, R.N., Morris, A.P., Smart, K.J., Sickman, Z.T., Bentz, M., Lehrmann, D., Evans, M.A., 2014. Control of mechanical stratigraphy on bed-restricted jointing and normal faulting: Eagle Ford Formation, south-central Texas. AAPG (Am. Assoc. Pet. Geol.) Bull. 98 (11), 2477–2506. https://doi.org/10.1306/08191414053.
Fitzgerald, P.G., Malusà, M.G., 2018. Concept of the Exhumed Partial Annealing (Retention) Zone and Age-Elevation Profiles in Thermochronology. Springer International Publishing, Cham, pp. 165–189.
Flowers, R.M., Ketcham, R.A., Shuster, D.L., Farley, K.A., 2009. Apatite (U-Th)/He thermochronometry using a radiation damage accumulation and annealing model. Geochem. Cosmochim. Acta 73 (8), 2347–2365. https://doi.org/10.1016/j.gca.2009.01.015.
Flowers, R.M., Shuster, D.L., Wernicke, B.P., Farley, K.A., 2007. Radiation damage control on apatite (U-Th)/He dates from the Grand Canyon region, Colorado Plateau. Geology 35 (5), 447. https://doi.org/10.1130/G23471A.1.
Galbraith, R.F., 1981. On statistical models for fission track counts. Math. Geol. 6 (13), 471–478.
Galibraith, R.F., Green, P.F., 1990. Estimating the component ages in a finite mixture. Nucl. Tracks Radiat. Meas. 3 (17), 197–206.
Ge, X., Hu, W., Ma, Y., Li, M., Tang, J., Zhao, P., 2021. Quantitative evaluation of geological conditions for shale gas preservation based on vertical and lateral constraints in the Songkan area, Northern Guizhou, southern China. Mar. Petrol. Geol. 124, 104787 https://doi.org/10.1016/j.marpetgeo.2020.104787.
Gleadow, A., Harrison, M., Kohn, B., Lugo-Zazueta, R., Phillips, D., 2015. The Fish Canyon Tuff: a new look at an old low-temperature thermochronology standard. Earth Planet Sci. Lett. 424, 95–108. https://doi.org/10.1016/j.epsl.2015.05.003.
Gleadow, A.J.W., Duddy, I.R., Green, P.F., Hegarty, K.A., 1986. Fission track lengths in the apatite annealing zone and the interpretation of mixed ages. Earth Planet Sci. Lett. 78 (2), 245–254. https://doi.org/10.1016/0012-821X(86)90065-8.
Green, P.F., Crowhurst, P.V., Duddy, I.R., Japsen, P., Holford, S.P., 2006. Conflicting (U-Th)/He and fission track ages in apatite: enhanced He retention, not anomalous annealing behaviour. Earth Planet Sci. Lett. 250 (3–4), 407–427. https://doi.org/10.1016/j.epsl.2006.08.022.
Green, P.F., Duddy, I.R., Gleadow, A.J.W., Tingate, P.R., Laslett, G.M., 1986. Thermal annealing of fission tracks in apatite: 1. A qualitative description. Chem. Geol. Isot. Geosci. 59, 237–253. https://doi.org/10.1016/0168-9622(86)90074-6.
Guenthner, W.R., Reiners, P.W., Ketcham, R.A., Nasdala, L., Giester, G., 2013. Helium diffusion in natural zircon: radiation damage, anisotropy, and the interpretation of zircon (U-Th)/He thermochronology. Am. J. Sci. 313 (3), 145–198. https://doi.org/10.2475/03.2013.01.
Guo, T.L., Zeng, P., 2015. The structural and preservation conditions for shale gas enrichment and high productivity in the Wufeng-Longmaxi Formation, Southeastern Sichuan Basin. Energy Explor. Exploit. 33 (3), 259–276. https://doi.org/10.1260/0144-5987.33.3.259.
Guo, X.S., Hu, D.F., Li, Y.P., Wei, Z.H., Wei, X.F., Liu, Z.J., 2017. Geological factors controlling shale gas enrichment and high production in Fuling shale gas field. Petrol. Explor. Dev. 44 (4), 513–523. https://doi.org/10.1016/S1876-3804(17)30060-5.
Hackley, P.C., Cardott, B.J., 2016. Application of organic petrography in North American shale petroleum systems: a review. Int. J. Coal Geol. 163, 8–51. https://doi.org/10.1016/j.coal.2016.06.010.
He, Z.L., Li, S.J., Nie, H.K., Yuan, Y.S., Wang, H., 2019. The shale gas "sweet window": "The cracked and unbroken" state of shale and its depth range. Mar. Petrol. Geol. 101, 334–342. https://doi.org/10.1016/j.marpetgeo.2018.11.033.
He, Z.L., Nie, H.K., Li, S.J., Luo, J., Wang, H., Zhang, G.R., 2020. Differential enrichment of shale gas in upper Ordovician and lower Silurian controlled by the plate tectonics of the Middle-Upper Yangtze, south China. Mar. Petrol. Geol. 118, 104357 https://doi.org/10.1016/j.marpetgeo.2020.104357.
Hu, D.F., Zhang, H.R., Ni, K., Yu, G.C., 2014. Preservation conditions for marine shale gas at the southeastern margin of the Sichuan Basin and their controlling factors. Nat. Gas. Ind. B 1 (2), 178–184. https://doi.org/10.1016/j.ngib.2014.11.009.
Hurford, A.J., Green, P.F., 1983. The zeta age calibration of fission track dating. Chem. Geol. 41, 285–317. https://doi.org/10.1016/s0009-2541(83)80026-6.
Jiang, G.Z., Hu, S.B., Shi, Y.Z., Zhang, C., Wang, Z.T., Hu, D., 2019. Terrestrial heat flow of continental China: updated dataset and tectonic implications. Tectonophysics 753, 36–48. https://doi.org/10.1016/j.tecto.2019.01.006.
Ju, Y.W., Sun, Y., Tan, J.Q., Bu, H.L., Han, K., Li, X.S., Fang, L.Z., 2018. The composition, pore structure characterization and deformation mechanism of coal-bearing shales from tectonically altered coalfields in eastern China. Fuel 234, 626–642. https://doi.org/10.1016/j.fuel.2018.06.116.
Julia, F.W.G., Stephen, E.L., Jon, E.O., Peter, E., Fall, A., 2014. Natural Fractures in shale: a review and new observations. AAPG (Am. Assoc. Pet. Geol.) Bull. 98 (11), 2165–2216. https://doi.org/10.1306/08121413151.
Ketcham, R.A., 2005. Forward and inverse modeling of low-temperature thermochronometry data. Rev. Mineral. Geochem. 58 (1), 275–314. https://doi.org/10.2138/rmg.2005.58.11.
Ketcham, R.A., Carter, A., Donelick, R.A., Barbarand, J., Hurford, A.J., 2007. Improved modeling of fission-track annealing in apatite. Am. Mineral. 92 (5–6), 799–810. https://doi.org/10.2138/am.2007.2281.
Li, C.X., He, D.F., Sun, Y.P., He, J.Y., Jiang, Z.X., 2015. Structural characteristic and origin of intra-continental fold belt in the eastern Sichuan basin, South China Block. J. Asian Earth Sci. 111, 206–221. https://doi.org/10.1016/j.jseaes.2015.07.027.
Li, J., Zhou, S.X., Gaus, G., Li, Y.J., Ma, Y., Chen, K.F., Zhang, Y.H., 2018. Characterization of methane adsorption on shale and isolated kerogen from the Sichuan Basin under pressure up to 60 MPa: experimental results and geological implications. Int. J. Coal Geol. 189, 83–93. https://doi.org/10.1016/j.coal.2018.02.020.
Li, J.H., Zhang, Y.Q., Dong, S.W., Johnston, S.T., 2014. Cretaceous tectonic evolution of South China: a preliminary synthesis. Earth Sci. Rev. 134, 98–136. https://doi.org/10.1016/j.earscirev.2014.03.008.
Li, J.H., Zhang, Y.Q., Zhao, G.C., Johnston, S.T., Dong, S.W., Koppers, A., Miggins, D.P., Sun, H.S., Wang, W.B., Xin, Y.J., 2017. New insights into phanerozoic tectonics of south China: early paleozoic sinistral and triassic dextral transpression in the east wuyishan and chencai domains, NE cathaysia. Tectonics 36 (5), 819–853. https://doi.org/10.1002/2016TC004461.
Li, S.J., Li, Y.Q., He, Z.L., Chen, K., Zhou, Y., Yan, D.T., 2020. Differential deformation on two sides of Qiyueshan Fault along the eastern margin of Sichuan Basin, China, and its influence on shale gas preservation. Mar. Petrol. Geol. 121, 104602 https://doi.org/10.1016/j.marpetgeo.2020.104602.
Li, X.M., Shan, Y.H., 2011. Diverse exhumation of the Mesozoic tectonic belt within the Yangtze Plate, China, determined by apatite fission-track thermochronology. Geosci. J. 15 (4), 349–357. https://doi.org/10.1007/s12303-011-0037-5.
Littke, R., Urai, J.L., Uffmann, A.K., Risvanis, F., 2012. Reflectance of dispersed vitrinite in Palaeozoic rocks with and without cleavage: implications for burial and thermal history modeling in the Devonian of Rursee area, northern Rhenish Massif, Germany. Int. J. Coal Geol. 89, 41–50. https://doi.org/10.1016/j.coal.2011.07.006.
Liu, R., Hao, F., Engelder, T., Zhu, Z.G., Yi, J.Z., Xu, S., Teng, C.Y., 2020. Influence of tectonic exhumation on porosity of Wufeng-Longmaxi shale in the Fuling gas field of the eastern Sichuan Basin, China. AAPG (Am. Assoc. Pet. Geol.) Bull. 104 (4), 939–959. https://doi.org/10.1306/08161918071.
Liu, S.F., Steel, R., Zhang, G.W., 2005. Mesozoic sedimentary basin development and tectonic implication, northern Yangtze Block, eastern China: record of continent-continent collision. J. Asian Earth Sci. 25 (1), 9–27. https://doi.org/10.1016/j.jseaes.2004.01.010.
Liu, S.G., Deng, B., Zhong, Y., Ran, B., Yong, Z.Q., Sun, W., Yang, D., Jiang, L., Ye, Y.H., 2016. Unique geological features of burial and superimposition of the Lower Paleozoic shale gas across the Sichuan Basin and its periphery. Earth Sci. Front. 23 (1), 22–28.
Liu, S.G., Yang, Y., Deng, B., Zhong, Y., Wen, L., Sun, W., Li, Z.W., Jansa, L.B., Li, J.X., Song, J.M., Zhang, X.H., Peng, H.L., 2021a. Tectonic evolution of the Sichuan Basin, southwest China. Earth Sci. Rev. 213, 103470 https://doi.org/10.1016/j.earscirev.2020.103470.
Liu, W., Qiu, N., Xu, Q., Liu, Y., 2018. Precambrian temperature and pressure system of Gaoshiti-Moxi block in the central paleo-uplift of Sichuan Basin, southwest China. Precambrian Res. 313, 91–108. https://doi.org/10.1016/j.precamres.2018.05.028.
Lu, W., Chou, I., Burruss, R.C., Song, Y., 2007. A unified equation for calculating methane vapor pressures in the CH_4-H_2O system with measured Raman shifts. Geochem. Cosmochim. Acta 71 (16), 3969–3978. https://doi.org/10.1016/j.gca.2007.06.004.
Luo, Q.Y., Fariborz, G., Zhong, N.N., Wang, Y., Qiu, N.S., Skovsted, C.B., Suchý, V., Hemmingsen Schovsbo, N., Morga, R., Xu, Y.H., Hao, J.Y., Liu, A.J., Wu, J., Cao, W. X., Min, X., Wu, J., 2020. Graptolites as fossil geo-thermometers and source material of hydrocarbons: an overview of four decades of progress. Earth Sci. Rev. 200, 103000 https://doi.org/10.1016/j.earscirev.2019.103000.
Ma, X.H., Wang, H.Y., Zhou, S.W., Shi, Z.S., Zhang, L.F., 2021. Deep shale gas in China: geological characteristics and development strategies. Energy Rep. 7, 1903–1914. https://doi.org/10.1016/j.egyr.2021.03.043.
Ma, Y.S., 2007. Marine Petroleum Exploration in China. Geological Press, Beijing (in Chinese).
Ma, Y.S., Cai, X.Y., Zhao, P.R., 2018. China's shale gas exploration and development: understanding and practice. Petrol. Explor. Dev. 45 (4), 589–603. https://doi.org/10.1016/S1876-3804(18)30065-X.
Masri, M., Sibai, M., Shao, J.F., Mainguy, M., 2014. Experimental investigation of the effect of temperature on the mechanical behavior of Tournemire shale. Int. J. Rock Mech. Min. Sci. 70, 185–191. https://doi.org/10.1016/j.ijrmms.2014.05.007.
Mei, L.F., Liu, Z.X., Tang, J.G., Shen, C.B., Fan, Y.F., 2010. Mesozoic intra-continental progressive deformation in western Hunan-Hubei-eastern Sichuan provinces of China: evidence from apatite fission track and balanced cross-section. Earth Sci. J. China Univ. Geosci. 35 (2), 161–174.
Nygård, R., Gutierrez, M., Bratli, R.K., Høeg, K., 2006. Brittle-ductile transition, shear failure and leakage in shales and mudrocks. Mar. Petrol. Geol. 23 (2), 201–212. https://doi.org/10.1016/j.marpetgeo.2005.10.001.
Ougier-Simonin, A., Renard, F., Boehm, C., Vidal-Gilbert, S., 2016. Microfracturing and microporosity in shales. Earth Sci. Rev. 162, 198–226. https://doi.org/10.1016/j.earscirev.2016.09.006.
Peng, D.Y., Robinson, D.B., 1976. A new two-constant equation of state. Ind. Eng. Chem. Res. 1 (15), 59–64.
Petersen, H.I., Schovsbo, N.H., Nielsen, A.T., 2013. Reflectance measurements of zooclasts and solid bitumen in Lower Paleozoic shales, southern Scandinavia: correlation to vitrinite reflectance. Int. J. Coal Geol. 114, 1–18. https://doi.org/10.1016/j.coal.2013.03.013.
Qiu, N.S., Feng, Q., Tenger, B., Shen, B.J., Ma, Z.L., Yu, L.J., Cao, A.Q., 2020. Yanshanian-himalayan differential tectono-thermal evolution and shale gas preservation in dingshan Area,Southeastern Sichuan Basin. Acta Pet. Sin. 41 (12), 1610–1622 (in Chinese with English abstract).

Qiu, N.S., Liu, W., Fu, X.D., Li, W.Z., Xu, Q.C., Qing, Z.C., 2021. Maturity evolution of lower cambrian qiongzhusi formation shale of the Sichuan Basin. Mar. Petrol. Geol. 128, 105061 https://doi.org/10.1016/j.marpetgeo.2021.105061.
Reiners, P.W., 2005. Zircon (U-Th)/He thermochronometry. Rev. Mineral. Geochem. 58 (1), 151–179. https://doi.org/10.2138/rmg.2005.58.6.
Reiners, P.W., Farley, K.A., 2001. Infuence of crystal size on apatite (U-Th)/He thermochronology: an example from the Bighorn Mountains, Wyoming. Earth Planet Sci. Lett. 188, 413–420. https://doi.org/10.1016/S0012-821X(01)00341-7.
Richardson, N.J., Densmore, A.L., Seward, D., Fowler, A., Wipf, M., Ellis, M.A., Yong, L., Zhang, Y., 2008. Extraordinary denudation in the Sichuan Basin: insights from low-temperature thermochronology adjacent to the eastern margin of the Tibetan Plateau. J. Geophys. Res. Solid Earth 113 (B4), B04409. https://doi.org/10.1029/2006JB004739.
Schloemer, S., Krooss, B.M., 2004. Molecular transport of methane. ethane and nitrogen and the influence of diffusion on the chemical and isotopic composition of natural gas accumulations 1 (4), 81–108. https://doi.org/10.1111/j.1468-8123.2004.00076.x.
Schmidt, J.S., Menezes, T.R., Souza, I.V.A.F., Spigolon, A.L.D., Pestilho, A.L.S., Coutinho, L.F.C., 2019. Comments on empirical conversion of solid bitumen reflectance for thermal maturity evaluation. Int. J. Coal Geol. 201, 44–50. https://doi.org/10.1016/j.coal.2018.11.012.
Shen, C.B., Mei, L.F., Xu, S.H., 2009. Fission track dating of Mesozoic sandstones and its tectonic significance in the Eastern Sichuan Basin, China. Radiat. Meas. 44 (9–10), 945–949. https://doi.org/10.1016/j.radmeas.2009.10.001.
Shi, H.C., Shi, X.B., Glasmacher, U.A., Yang, X.Q., Stockli, D.F., 2016. The evolution of eastern Sichuan basin, Yangtze block since Cretaceous: constraints from low temperature thermochronology. J. Asian Earth Sci. 116, 208–221. https://doi.org/10.1016/j.jseaes.2015.11.008.
Shu, Y., Lu, Y.C., Chen, L., Wang, C., Zhang, B.Q., 2020. Factors influencing shale gas accumulation in the lower Silurian Longmaxi formation between the north and South Jiaoshiba area, Southeast Sichuan Basin, China. Mar. Petrol. Geol. 111, 905–917. https://doi.org/10.1016/j.marpetgeo.2019.06.029.
Shuster, D.L., Flowers, R.M., Farley, K.A., 2006. The influence of natural radiation damage on helium diffusion kinetics in apatite. Earth Planet Sci. Lett. 249 (3–4), 148–161. https://doi.org/10.1016/j.epsl.2006.07.028.
Slatt, R.M., O'Brien, N.R., 2011. Pore types in the Barnett and Woodford gas shales: contribution to understanding gas storage and migration pathways in fine-grained rocks. AAPG (Am. Assoc. Pet. Geol.) Bull. 95 (12), 2017–2030. https://doi.org/10.1306/03301110145.
Smart, K.J., Ofoegbu, G.I., Morris, A.P., McGinnis, R.N., Ferrill, D.A., 2014. Geomechanical modeling of hydraulic fracturing: why mechanical stratigraphy, stress state, and pre-existing structure matter. AAPG (Am. Assoc. Pet. Geol.) Bull. 98 (11), 2237–2261. https://doi.org/10.1306/07071413118.
Spiegel, C., Kohn, B., Belton, D., Berner, Z., Gleadow, A., 2009. Apatite (U-Th-Sm)/He thermochronology of rapidly cooled samples: the effect of He implantation. Earth Planet Sci. Lett. 285 (1–2), 105–114. https://doi.org/10.1016/j.epsl.2009.05.045.
Sternai, P., Jolivet, L., Menant, A., Gerya, T., 2014. Driving the upper plate surface deformation by slab rollback and mantle flow. Earth Planet Sci. Lett. 405, 110–118. https://doi.org/10.1016/j.epsl.2014.08.023.
Suárez-Ruiz, I., Flores, D., Mendonça Filho, J.G., Hackley, P.C., 2012. Review and update of the applications of organic petrology: Part 1, geological applications. Int. J. Coal Geol. 99, 54–112. https://doi.org/10.1016/j.coal.2012.02.004.
Sweeney, J.J., Burnham, A.K., 1990. Evaluation of a simple model of vitrinite reflectance based on chemical kinetics. AAPG (Am. Assoc. Pet. Geol.) Bull. 74, 1559–1570.
Tan, P., Pang, H.W., Zhang, R.X., Jin, Y., Zhou, Y.C., Kao, J.W., Fan, M., 2020. Experimental investigation into hydraulic fracture geometry and proppant migration characteristics for southeastern Sichuan deep shale reservoirs. J. Petrol. Sci. Eng. 184, 106517 https://doi.org/10.1016/j.petrol.2019.106517.
Tang, S.L., Yan, D.P., Qiu, L., Gao, J.F., Wang, C.L., 2014. Partitioning of the cretaceous pan-yangtze basin in the central south China block by exhumation of the Xuefeng mountains during a transition from extensional to compressional tectonics? Gondwana Res. 25 (4), 1644–1659. https://doi.org/10.1016/j.gr.2013.06.014.
Taylor, G.H., Teichmqller, M., Davis, A., Diessel, C.F.K., Littke, R., Robert, P., 1998. Organic Petrology. Gebrqder Borntrager, Berlin.
Tian, H., Ziegler, M., Kempka, T., 2014. Physical and mechanical behavior of claystone exposed to temperatures up to 1000 °C. Int. J. Rock Mech. Min. Sci. 70, 144–153. https://doi.org/10.1016/j.ijrmms.2014.04.014.
Tian, Y.T., Kohn, B.P., Qiu, N.S., Yuan, Y.S., Hu, S.B., Gleadow, A.J.W., Zhang, P.Z., 2018. Eocene to Miocene out-of-sequence deformation in the eastern Tibetan plateau: insights from shortening structures in the Sichuan Basin. J. Geophys. Res. Solid Earth 123 (2), 1840–1855. https://doi.org/10.1002/2017JB015049.
Thomas, A.V., Pasteris, J.D., Bray, C.J., Spooner, E.T.C., 1990. H_2O-CH_4-NaCl-CO_2 inclusions from the footwall contact of the Tanco granitic pegmatite: estimates of internal pressure and composition from microthermometry, laser Raman spectroscopy, and gas chromatography. Geochem. Cosmochim. Acta 54 (3), 559–573. https://doi.org/10.1016/0016-7037(90)90353-m.
Tong, Y.B., Sun, Y.J., Wu, Z.H., Mao, C.P., Pei, J.L., Yang, Z.Y., Pu, Z.W., Zhao, Y., Xu, H., 2019. Passive crustal clockwise rotational deformation of the Sichuan Basin since the Miocene and its relationship with the tectonic evolution of the fault systems on the eastern edge of the Tibetan Plateau. Geol. Soc. Am. Bull. 131 (1–2), 175–190. https://doi.org/10.1130/B31965.1.
Vermeesch, P., 2009. RadialPlotter: a Java application for fission track, luminescence and other radial plots. Radiat. Meas. 44 (4), 409–410. https://doi.org/10.1016/j.radmeas.2009.05.003.
Vermeesch, P., 2012. On the visualisation of detrital age distributions. Chem. Geol. 312–313, 190–194. https://doi.org/10.1016/j.chemgeo.2012.04.021.
Vermeesch, P., Seward, D., Latkoczy, C., Wipf, M., Günther, D., Baur, H., 2007. α-Emitting mineral inclusions in apatite, their effect on (U-Th)/He ages, and how to reduce it. Geochem. Cosmochim. Acta 71 (7), 1737–1746. https://doi.org/10.1016/j.gca.2006.09.020.
Wang, E., Meng, K., Su, Z., Meng, Q.G., Chu, J.J., Chen, Z.L., Wang, G., Shi, X., Liang, X.Q., 2014. Block rotation: tectonic response of the Sichuan basin to the southeastward growth of the Tibetan Plateau along the Xianshuihe-Xiaojiang fault. Tectonics 33 (5), 686–718. https://doi.org/10.1002/2013TC003337.
Wang, X., Chou, I.M., Hu, W., Burruss, R.C., Sun, Q., Song, Y., 2011. Raman spectroscopic measurements of CO_2 density: experimental calibration with high-pressure optical cell (HPOC) and fused silica capillary capsule (FSCC) with application to fluid inclusion observations. Geochem. Cosmochim. Acta 75 (14), 4080–4093. https://doi.org/10.1016/j.gca.2011.04.028.
Wang, Y., Qiu, N.S., Borjigin, T., Shen, B.J., Xie, X.M., Ma, Z.L., Lu, C.J., Yang, Y.F., Yang, L., Cheng, L.J., Fang, G.J., Cui, Y., 2019. Integrated assessment of thermal maturity of the upper ordovician-lower silurian wufeng-longmaxi shale in Sichuan Basin, China. Mar. Petrol. Geol. 100, 447–465. https://doi.org/10.1016/j.marpetgeo.2018.10.025.
Wang, Y., Qiu, N.S., Xie, X.M., Ma, Z.L., Li, L.L., Feng, Q.Q., Yang, L., Shen, B.J., Borjigin, T., Tao, N., 2021. Maturity and thermal evolution differences between two sets of Lower Palaeozoic shales and its significance for shale gas formation in south-western Sichuan Basin, China. Geol. J. 56 (7), 3698–3719. https://doi.org/10.1002/gj.4121.
Wei, L., Wang, Y.Z., Mastalerz, M., 2016. Comparative optical properties of macerals and statistical evaluation of mis-identification of vitrinite and solid bitumen from early mature Middle Devonian-Lower Mississippian New Albany Shale: implications for thermal maturity assessment. Int. J. Coal Geol. 168, 222–236. https://doi.org/10.1016/j.coal.2016.11.003.
Wei, X.F., Li, Y.P., Wei, Z.H., Liu, R.B., Yu, G.C., Wang, Q.B., 2017. Effects of preservation conditions on enrichment and high yield of shale gas in Sichuan Basin and its periphery. Petroleum Geology & Experiment 39 (2), 147–153.
Wilkins, S., Mount, V., Mahon, K., Perry, A., Koenig, J., 2014. Characterization and development of subsurface fractures observed in the Marcellus Formation, Appalachian Plateau, north-central Pennsylvania. AAPG (Am. Assoc. Pet. Geol.) Bull. 98 (11), 2301–2345. https://doi.org/10.1306/08191414024.
Wolf, R.A., FK, A.K., 1998. Modeling of the temperature sensitivity of the apatite (U-Th)/He thermochronometer. Chem. Geol. 1–2 (148), 105–114.
Wu, H., 2019. Meso-Cenozoic Tectonic Uplift Process of the Eastern Sichuan Basin. China University of Petroleum, Beijing (in Chinese).
Wu, H., Qiu, N., Feng, Q., Chang, J., Jiang, K., Zhang, Y., Wu, S., 2020. Reconstruction of tectonic uplift process with thermo-kinematic method. Chinese. Chin. J. Geophys. 63 (6), 2329–2344 (in Chinese with English abstract).
Xu, M., Zhu, C.Q., Tian, Y.T., Rao, S., Hu, S.B., 2011. Borehole temperature logging and characteristics of subsurface temperature in the Sichuan Basin. Chin. J. Phys. 54 (4), 1052–1060. https://doi.org/10.3969/j.issn.0001-5733.2011.04.020.
Xu, Q.C., Qiu, N.S., Liu, W., Shen, A.J., Wang, X.F., 2018. Thermal evolution and maturation of sinian and cambrian source rocks in the central Sichuan Basin, southwest China. J. Asian Earth Sci. 164, 143–158. https://doi.org/10.1016/j.jseaes.2018.06.015.
Yamada, R., Murakami, M., Tagami, T., 2007. Statistical modelling of annealing kinetics of fission tracks in zircon; Reassessment of laboratory experiments. Chem. Geol. 236 (1–2), 75–91. https://doi.org/10.1016/j.chemgeo.2006.09.002.
Yan, D.P., Zhou, M.F., Song, H.L., Wang, X.W., Malpas, J., 2003. Origin and tectonic significance of a mesozoic multi-layer over-thrust system within the Yangtze block (south China). Tectonophysics 361 (3–4), 239–254. https://doi.org/10.1016/S0040-1951(02)00646-7.
Yang, H.J., Han, X., Wang, L., 2021. Is there a bubble in the shale gas market? Energy 215, 119101. https://doi.org/10.1016/j.energy.2020.119101.
Yong, T., Fan, Y., Lv, Q.Q., Tang, W.J., Wang, H.K., 2018. Analysis of the tectonic stress field of SE sichuan and its impact on the preservation of shale gas in lower silurian longmaxi formation of the dingshan region, China. J. Geol. Soc. India 92, 92–100. https://doi.org/10.1007/s12594-018.
Yu, L.J., Fan, M., Borjigin, T., Liu, Y.X., 2016. Shale gas occurrence under burial conditions. Petroleum Geology & Experiment 38 (4), 438–444. https://doi.org/10.11781/sysydz201604438.
Yuan, Y.S., Jin, Z.J., Zhou, Y., Liu, J.X., Li, S.J., Liu, Q.Y., 2017. Burial depth interval of the shale brittle-ductile transition zone and its implications in shale gas exploration and production. Petrol. Sci. 14 (4), 637–647. https://doi.org/10.1007/s12182-017-0189-7.
Yuan, Y.S., Sun, D.S., Zhou, Y., Wang, X.W., Li, S.J., Zhang, R.Q., Wo, Y.J., 2010. Determination of onset of uplifting for the Mid-upper Yangtze area after Indosinian event. Chin. J. Geophys. 53 (2), 362–369 (in Chinese with English abstract).
Zeng, W.T., Zhang, J.C., Ding, W.L., Zhao, S., Zhang, Y.Q., Liu, Z.J., Jiu, K., 2013. Fracture development in Paleozoic shale of Chongqing area (South China). Part one: fracture characteristics and comparative analysis of main controlling factors. J. Asian Earth Sci. 75, 251–266. https://doi.org/10.1016/j.jseaes.2013.07.014.
Zeng, Y.J., Chen, Z., Bian, X.B., 2016. Breakthrough in staged fracturing technology for deep shale gas reservoirs in SE Sichuan Basin and its implications. Nat. Gas. Ind. B 3 (1), 45–51. https://doi.org/10.1016/j.ngib.2016.02.005.
Zhang, Y.G., Frantz, J.D., 1987. Determination of the homogenization temperatures and densities of supercritical fluids in the system NaCl-KCl-CaCl2-H2O using synthetic fluid inclusions. Chem. Geol. 3 (64), 335–350. https://doi.org/10.1016/0009-2541(87)90012-X.

Zhu, H.J., Ju, Y.W., Huang, C., Chen, F.W., Chen, B.Z., Yu, K., 2020. Microcosmic gas adsorption mechanism on clay-organic nanocomposites in a marine shale. Energy 197, 117256. https://doi.org/10.1016/j.energy.2020.117256.

Zou, C.N., Yang, Z., Dai, J.X., Dong, D.Z., Zhang, B.M., Wang, Y.M., Deng, S.H., Huang, J. L., Liu, K.Y., Yang, C., Wei, G.Q., Pan, S.Q., 2015. The characteristics and significance of conventional and unconventional Sinian-Silurian gas systems in the Sichuan Basin, central China. Mar. Petrol. Geol. 64, 386–402. https://doi.org/10.1016/j.marpetgeo.2015.03.005.

Northrup, C. J., Royden, L. H., Burchfiel, B. C., 1995. Motion of the Pacific Plate relative to Eurasia and its potential relation to Cenozoic extension along the eastern margin of Eurasia. Geology 23(8), 719–722. doi:10.1130/0091–7613(1995)023<0719:MOTPPR>2.3.CO;2.